BeFo
STIFTELSEN BERGTEKNISK FORSKNING
ROCK ENGINEERING RESEARCH FOUNDATION

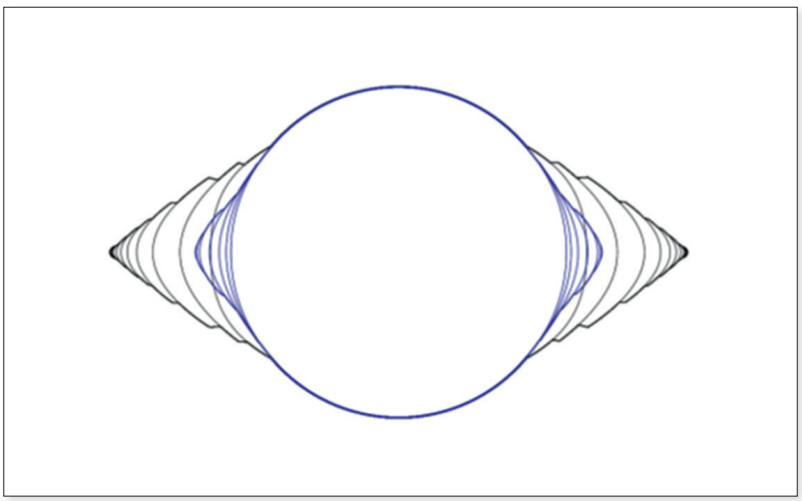

A NOVEL SEMI-ANALYTICAL TOOL FOR STRESS INTERPRETATION USING BOREHOLE BREAKOUTS

Eleni Gerolymatou
Åsa Fransson

BeFo Report 211

Figure 43: Breakout shape for the initial guesses. It can be seen that while the width is the same, the depth is very different. Moreover, in contrast to the small-scale simulation, the breakouts are dog-ear shaped instead of cusp shaped.

STIFTELSEN BERGTEKNISK FORSKNING
ROCK ENGINEERING RESEARCH FOUNDATION

A NOVEL SEMI-ANALYTICAL TOOL FOR STRESS INTERPRETATION USING BOREHOLE BREAKOUTS

Ett nytt semi-analytiskt verktyg för spänningstolkning baserad på borrhålsutfall

Eleni Gerolymatou, Chalmers University of Technology

Åsa Fransson, Golder Associates/University of Gothenburg

BeFo Report 211
Stockholm 2020
ISSN 1104-1773
ISRN BEFO-R-211-SE

PREFACE

The ability to describe and predict the stability of a borehole and to have a possibility to assess the in situ stress state is relevant for a large number of applications. These include but are not limited to tunneling, the storage of nuclear waste, energy applications, such as gas production and hydrothermal energy and mining.

The semi-analytical tool that is presented in this report has been shown to agree well with experimental results and is significantly faster than the more precise but unsuitable for brittle rock finite element simulations of the same problem. It is therefore hoped that it will provide a simple and easy to use tool for applications involving excavations in rock, with emphasis on the field of civil engineering and energy production.

The work has mainly been carried out by Eleni Gerolymatou, Chalmers University of Technology, in collaboration with Åsa Fransson, Golder Associates and University of Gothenburg (focusing on the concluding part where data from a previously conducted field test has been used). The project's reference group consisted of Diego Mas Ivars, SKB, Jonny Sjöberg, Itasca, Thomas Wettainen, LKAB and Per Tengborg, BeFo. In addition, the report was reviewed by Lars-Olof Dahlström, Golder Associates. The project was funded by BeFo, Rock Engineering Research Foundation.

Stockholm, 2020
Per Tengborg

FÖRORD

Att kunna beskriva och förutsäga ett borrhåls stabilitet och att kunna bedöma dess spänningstillstånd är relevant för ett stort antal tillämpningar. Dessa inkluderar men är inte begränsade till drivning av tunnlar, lagring av kärnavfall, energitillämpningar, såsom gasproduktion och hydrotermisk energi, och gruvdrift.

Det semi-analytiska verktyg som presenteras i denna rapport har visat sig överensstämma väl med experimentella resultat och är betydligt snabbare än finitelementsimuleringar som kan vara mer exakta men som då också är både svårare att kalibrera och mer besvärliga att utföra. Förhoppningen är att detta kommer att vara ett enkelt och lättanvänt verktyg för tillämpningar som involverar tunneldrivning i berg, med tyngdpunkt på samhällsbyggnad, anläggning och energiproduktion.

Arbetet har i huvudsak genomförts av Eleni Gerolymatou, Chalmers tekniska högskola, i samverkan med Åsa Fransson, Golder Associates och Göteborgs universitet (med fokus på den avslutande delen där underlag från ett tidigare utfört fältförsök har använts). Projektets referensgrupp har bestått av Diego Mas Ivars, SKB, Jonny Sjöberg, Itasca, Thomas Wettainen, LKAB och Per Tengborg, BeFo. Rapporten har även granskats av Lars-Olof Dahlström, Golder Associates. Projektet har finansierats av BeFo, Stiftelsen Bergteknisk Forskning.

Stockholm, 2020
Per Tengborg

SUMMARY

The present report describes a methodology developed within the frame of the BEFO project 408 for two applications. The first one concerns the prediction of the shape of borehole breakouts when the material properties and the *in situ* stress state is known. The second concerns the assessment of the *in situ* stress state when the material properties and the shape of the borehole breakouts is known. Both the possibility of being able to predict the stability of a borehole and the possibility of being able to assess the *in situ* stress state are relevant for a large number of applications. These include but are not limited to tunneling, including the smaller boreholes created for anchoring and blasting, the storage of nuclear waste, energy applications, such as gas production and hydrothermal energy and mining.

The concept presented here is based on the method of conformal mapping. Conformal mapping is based on complex analysis and was initially applied to the solution of flow problems, most notable aerodynamics. In the field of civil engineering the method is most commonly used for the solution of groundwater flow problems with the approach of flow nets. In this report, the theory of conformal mapping, as well as the numerical methods used and their development, are presented in chapter 4 for the interested reader. With the possible exception of the sections referring to examples, reading this chapter is not necessary for most readers.

The main results for the evaluation of the shape of the borehole breakouts are presented in chapters 5 and 6, while the main results for the evaluation of the *in situ* stress state are presented in chapter 7. Chapter 8 aims to provide an example for the application suggested here to real project data. The data used originate from the BRIE project, standing for Bentonite Rock Interaction Experiment and funded by SKB. For the needs of this project boreholes were cored in crystalline, granitic rock and subsequently bentonite parcels were installed. The whole construct was subsequently overcored for further testing and observation. Fracture mapping both before and after the introduction of bentonite is available, as well as estimates of the *in situ* stress state. Chapter 9 closes the report with conclusions, some observations and possible future extensions.

The method that is presented here has been shown to agree well with experimental results and is significantly faster than the more precise but harder to calibrate and more cumbersome finite element simulations of the same problem. It is therefore hoped that it will provide a simple and easy to use tool for applications involving excavations in rock, with emphasis on the field of civil engineering and energy production.

Keywords: *in situ* stress, borehole breakouts, rock stability, brittle failure

SAMMANFATTNING

Föreliggande rapport beskriver en metod som utvecklats inom ramen för BEFO-projekt 408 och för två olika applikationer. Den första handlar om förutsägelse av geometri för borrhålsutfall när materialegenskaper och spänningstillstånd *in situ* är kända. Den andra avser bedömning av spänningstillstånd när materialegenskaper och geometri för borrhålsutfall är kända. Både möjligheten att kunna förutsäga stabiliteten i ett borrhål och möjligheten att kunna bedöma spänningstillståndet är relevanta för ett stort antal tillämpningar. Dessa inkluderar men är inte begränsade till drivning av tunnlar, inklusive de mindre borrhål som används för förankring och sprängning, lagring av kärnavfall, energitillämpningar, såsom gasproduktion och hydrotermisk energi, och gruvdrift.

Konceptet som presenteras här är baserat på metoden för *"conformal mapping"*. *"Conformal mapping"* är baserad på komplex analys och applicerades initialt på lösningen av flödesproblem, exempelvis aerodynamik. Inom samhällsbyggande används metoden oftast för att lösa problem med grundvattenflöden (med hjälp av flödesnät). I kapitel 4 i denna rapport presenteras teorin för *"conformal mapping"* och använda numeriska metoder och deras utveckling. Förutom de avsnitt som hänvisar till exempel är detta kapitel att betrakta som en fördjupning för den mer intresserade läsaren.

De viktigaste resultaten relaterade till utvärdering av geometri för borrhålsutfall presenteras i kapitel 5 och 6, medan de viktigaste resultaten för utvärdering av spänningstillstånd *in situ* presenteras i kapitel 7. Kapitel 8 syftar till att bedöma och ge exempel på användbarheten för verkliga fältdata. Data kommer från projektet BRIE, Bentonite Rock Interaction Experiment, som har drivits och finansierats av SKB. För detta projekt borrades borrhål i kristallint berg och bentonit installerades sedan i borrhålen. Genom borrning och vajersågning lyftes både berg och bentonit sedan upp för ytterligare observationer och tester. Såväl sprickkartering före och efter installation av bentonit som skattningar av spänningstillstånd *in situ* finns att tillgå för försöksplatsen. Kapitel 9 avslutar rapporten med slutsatser, några observationer och möjligheter till framtida utveckling av metoden.

Metoden som presenteras här har visat sig överensstämma väl med experimentella resultat och är betydligt snabbare än finitelementsimuleringar som kan vara mer exakta men som då också är både svårare att kalibrera och mer besvärliga att utföra. Förhoppningen är att detta kommer att vara ett enkelt och lättanvänt verktyg för tillämpningar som involverar tunneldrivning i berg, med tyngdpunkt på samhällsbyggnad, anläggning och energiproduktion.

Nyckelord: *in situ* spänningar, borrhålsutfall, bergsstabilitet, sprött brott

TABLE OF CONTENTS

1. INTRODUCTION

Boreholes and other cavities of a circular cross-section are relevant to a wide variety of applications, such as tunneling, geothermal energy production, oil and gas production, nuclear waste disposal and stress measurement, with various methods such as overcoring, hydrofracturing or through the interpretation of borehole breakouts. Breakouts are of importance in all above applications, both as a threat to borehole or tunnel stability and as a tool for the primary stress state interpretation. The necessary simulations are challenging from a numerical point of view, as the problem is linked to loss of numerical stability for ductile rock and loss of continuity for brittle rock. The first case can be tackled using advanced continuum formulations, such as micropolar of nonlocal models (Noll, 1972), to model the material behavior. The second is more challenging and no continuum-based solutions are currently available.

The present project presents a semi-analytical method for both the prediction of breakouts in brittle rock and their use to assess the primary *in situ* stress. The project is subdivided into three steps. In the first, a tool is developed for the prediction of the form and size of the breakouts for given primary stresses and material parameters. The correctness is verified by means of comparison to analytical solutions. In the second step, using also the method developed in the first step, a tool is developed for the estimation of the primary *in situ* stress for given geometries of the borehole breakouts and given material properties. Finally, the applicability and efficiency of both resulting tools is validated against data from the literature and field experiments, with focus on the BRIE (Bentonite Rock Interaction Experiment) project. The aim is to provide a simple, fast and easy to use tool for the assessment of borehole and tunnel stability and for the estimation of the *in situ* stress in brittle rock.

1.1 Project background

As already mentioned, boreholes and other cavities of a circular cross-section are relevant to a wide variety of applications. Breakouts are local failures observed at the wall of the cavity and can vary strongly in shape and intensity. Examples are shown in Figure 1. From left to right one sees (a) Spiral failure pattern in Posidonia slate under isotropic stress after (Meier et al., 2013), (b) Dog-ear breakout in Westerly granite under anisotropic stress after (Song & Haimson, 1997) and (c) Slit shaped breakout in Berea sandstone under anisotropic stress state with a high mean pressure after (Haimson & Kovacich, 2003). Similar effects have been directly observed in tunnels and shafts.

Shear and compaction induced breakouts tend to orient themselves parallel to the minimum principal stress. Tensile breakouts, in the form of cracks, tend to orient themselves normal to minimum principal stress. Deviations from this orientation are rare

but have been observed in intensely anisotropic rocks, such as shale (Choens, Lee, Ingraham, Dewers, & Herrick, 2019).

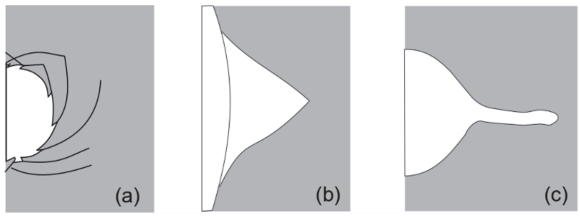

Figure 1. Different types of borehole wall failure (a) shear spirals modified after (Meier, Rybacki, Reinicke, & Dresen, 2013), (b) dog ear breakout modified after (Song & Haimson, 1997), (c) slit shaped compression breakout modified after (Haimson & Kovacich, 2003).

Breakouts are of importance both as a threat to borehole or tunnel stability and as a tool for the primary stress state interpretation. For the interpretation of the primary *in situ* stress, the breakouts are logged along the depth of unlined boreholes. Several techniques are available, such as optical, acoustic (ultrasound) and electrical resistance imaging. A further popular method involves data from four arm caliper tools, used widely in the hydrocarbon industry. The orientation and type of the breakouts provides information concerning the orientation of the principal stresses. Breakout orientations can rotate in inclined boreholes and may not always directly yield the horizontal stress orientations. It is therefore considered preferable to estimate the maximum horizontal stress from breakouts in approximately vertical boreholes, with a deviation from the vertical that is smaller than 10°. In order to derive information concerning the magnitude of the principal stresses, analytical elastic solutions, mostly the solution introduced by Michell (Michell, 1899), are used as a rule. Solutions like this do not take into account the redistribution of stresses as the failure progresses. When the breakouts are shear induced, a domain can be determined with these solutions in which the stress state is likely to be, assuming frictional failure in the material. This is possible, due to the fact that the width of the breakouts

remains constant during the procedure of the breakout formation, as shown by (Zoback et al., 2003), see Figure 2. The material tested in this case was limestone.

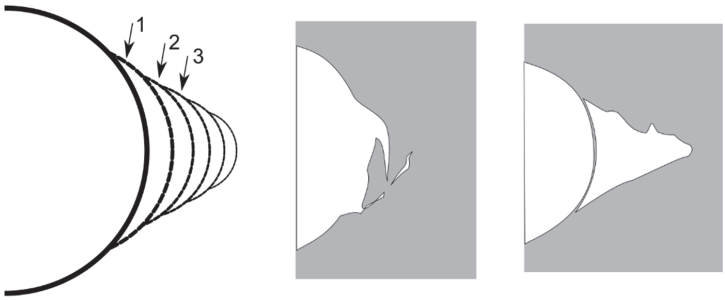

Figure 2. Evolution of borehole breakouts, experimental images on the right modified after (Zoback et al., 2003).

A set of ranges, rather than a value, of stresses is determined, because the depth of the breakout cannot be utilized without considering stress rearrangement. For compressive and tensile modes of failure the width cannot be utilized either, due to the form of the breakouts, so that only the orientation can be recovered from the data.

As far as energy production is concerned, following the state of practice, the first part of boreholes is drilled starting with a larger radius and reducing diameter with increasing depth. This is required by the placement of the casing, stabilizing the borehole against collapse and protecting both borehole and surrounding formation from the circulating fluid. Newer technologies allow for a section before branching with constant radius. The lower part of production boreholes exhibits branching, often in the horizontal or sub-horizontal direction. In the majority of cases this portion of the hole does not have a casing, to allow fluid circulation by means of a pressure gradient and is thus particularly exposed to failure. Production boreholes have an average depth of about 2000 m, so that failures are particularly costly.

Borehole breakouts are also of importance for fossil fuel production, because they influence sand production, which in turn influences the lifetime of the borehole and the machinery and the rate of production. A further domain of interest is nuclear waste disposal, as time-delayed formation of breakouts can form preferential pathways for groundwater. Beyond this, smaller boreholes are often part of engineering projects, either

as a part of the site investigation or as a part of the construction process, for example when bolting or blasting.

Last but not least, breakouts also occur in civil and in mining applications, both in the smaller scale of the boreholes constructed for bolting, for blasting and for site investigation, and in the large scale of tunnels and shafts.

1.2 Project purpose

Within the frame of this project, a simple and easy to use semi-analytical tool is proposed for brittle rock or for cases where the breakout material is detached from the borehole wall. The assumption is made, that the material is elastic up to the point of failure and removed from the cavity wall after this. The problem is thus reduced to the evaluation of the stress state around a cavity with an arbitrary, i.e. non-circular, shape. To this end conformal mapping (Schinzinger & Laura, 2003) will be used. This technique has been used for several decades for the estimation of the stress distribution of plane problems with a complex geometry, especially in fracture mechanics. If the stress distribution is known, the domains where failure takes place can be pinpointed and removed from the configuration. In that way, the geometry of the cavity converges to the final one. The evaluation of the stresses is analytical, but the evaluation of the mapping needs to be performed numerically. Thus, the method can be termed as semi-analytical.

Once the forward problem is solved, i.e. the evaluation of the shape of the breakouts for known principal stress state, the backward problem can be solved as well, in the form of an optimization procedure. The task is to find the principal stresses, when the breakout geometry is known. Thus, it is enough to pinpoint the value of the principal stresses that yields the optimal fit between theoretical and measured results.

Since the method is based on elasticity and conformal mapping, it does not require time integration, very fine discretization or a large number of iterations. It is therefore to be expected that it will possess a very low computational cost.

A further advantage is the very wide range of materials to which it is applicable. The method can be used on all brittle rocks, including granites, shales, limestones and sandstones. The parameters of the failure criterion only need to be adjusted accordingly, for example the uniaxial strength and the parameter m, if the Hoek-Brown criterion is used. The method cannot be applied only in the case that the failure is ductile.

Local perturbations in strength, for example local strength reduction in the vicinity of the borehole, due to drilling induced damage, and anisotropy in strength, can be easily incorporated in the formulation, as the method requires only uniformity in the elastic properties and not in the failure criteria. Anisotropy in the elastic properties can also be taken into account using conformal mapping, see for example (Schinzinger & Laura, 2003), but is not within the scope of this project, because the anisotropy of the elastic

properties of the material *in situ* is in practice often not known. Heterogeneity in the elastic properties cannot be taken into account, unless using much more complex numerical approaches.

A foreseeable drawback is that the resulting tool cannot take into account local stress perturbations due to single, discrete fractures in the vicinity of the borehole, unless these intersect the borehole. In this case, the tool will yield the stress field including the perturbation in the stress field caused by the fractures, as it is this stress state that governs the shape of the borehole breakouts. If the fractures intersect the borehole they can be included in the initial geometry of the borehole, which does not need to be circular.

Though this method has been rarely used to evaluate the stress state around non-circular openings in rock engineering (Exadaktylos, Liolios, & Stavropoulou, 2003; Kargar, Rahmannejad, & Hajabasi, 2015), it has never been applied to the progressive formation of borehole breakouts or to the estimation of the *in situ* stress.

1.3 Report outline

The present report consists of a total of nine chapters, with the present chapter serving as an introduction. The second chapter contains a literature review on different aspects of the observation and simulation of borehole breakouts. Topics linked to observation that are discussed include the observation of their formation, both on the situ and under controlled conditions in the laboratory, the mechanics of their formation and arrest. Methods currently used for their prediction and simulation are also discussed and the approach commonly used for the assessment of the *in situ* stress state is briefly outlined.

The general methodology is outlined in chapter 3. This chapter summarizes the underlying assumptions of the method and its limitations and presents an outline of the algorithms used. The theory and developed method used for the prediction of the shape of borehole breakouts are presented in chapter 4. This chapter includes the mathematical theory and background of the method, as well as details of the implementation, that may only be of interest to a small number of readers. For the majority of readers, the perusal of this chapter is not necessary and the description of the algorithms, presented in chapter 3, is sufficient to follow the rest of the contents.

Chapters 5 to 7 present results of the numerical implementations performed. The first two are concerned with the prediction of the shape of the borehole breakouts, while the third is concerned with the assessment of the *in situ* stress state. As the series expansions used in the approximation of the geometry leads to some small oscillations, some form of regularization is necessary. Two alternatives are presented. In chapter 5 a moving average is used, while in chapter 6 an interpolation is used. In chapter 6 scale effects are also introduced.

In chapter 8 an attempt is made to assess the applicability of the presented method to real data. The information used comes from the BRIE (Bentonite Rock Interaction Experiment), where a number of well documented boreholes were created and filled with bentonite. Due to the uncertainties in the input, the results are presented in the form of a parametric analysis.

The last chapter, chapter 9, contains a discussion on the presented results, some conclusions concerning the method and some thoughts on future work.

2. LITERATURE REVIEW

In this chapter a literature review of the different aspects of the project is presented. The different aspects are discussed separately but are not necessarily unrelated. Observations both *in situ* and in the laboratory are discussed first, with a separate section devoted to breakout arrest. The existing efforts at prediction and simulation of the formation breakouts follow and the state of practice for the use of borehole breakouts to assess the *in situ* stress state closes the chapter.

2.1 *In situ* observations and laboratory tests

Breakouts have been observed both on site and in the laboratory. *In situ* observations refer to boreholes, shafts and tunnels, with the best documented case for the last two being the Underground Research Laboratory, constructed in granite in Pinawa, Manitoba. The *in situ* stress is estimated in (Haimson, Lee, Chandler, & Martin, 1993). It is concluded that the vertical stress varies between 12.0 and 13.5 MPa, the maximum horizontal is in the range σ_H = 54 +/- 13 MPa and the minimum horizontal in the range σ_h = 36 +/- 16 MPa at a depth ranging from 450.7 m and 510.8 m. Breakouts in tunnels and shafts with a sub-horizontal direction were observed, aligned approximately in the vertical direction.

Observations in the laboratory offer the advantage that the boundary conditions and the material properties are known or can be measured. Usually the borehole breakout and width are measured, as shown in Figure 3, at different initial stresses. The breakout width is characterized by the aperture angle θ, while the depth is measured from the center of the borehole and is symbolized with d in the figure.

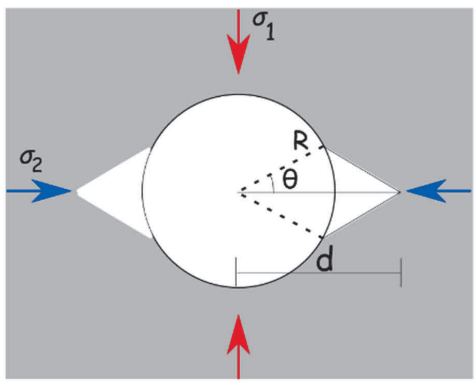

Figure 3. Breakout geometry.

As mentioned in the introduction, depending on the stress state the shape of the breakout varies, as shown in Figure 1. An example of the dependence of the width and the depth

of breakouts for Tablerock sandstone on the stress state is given in Figure 4 after (Haimson & Lee, 2004). The breakouts observed were of the dog-ear type and it can be observed that increasing stress ratio leads to both increasing depth and width of the breakouts.

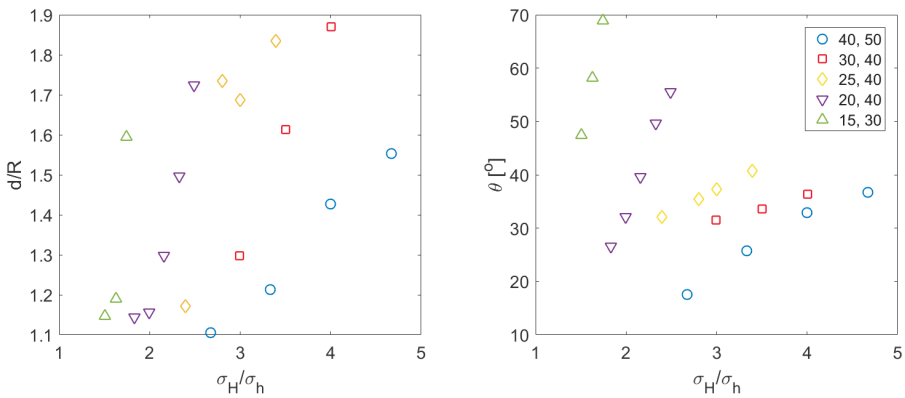

Figure 4. Breakout depth and width for Tablerock sandstone after (Haimson & Lee, 2004). The first column of the legend gives the minimum horizontal stress and the second gives the vertical stress. The boreholes were bored in the vertical direction.

The type of rock also affects the type of breakout. High porosity rocks have higher probability of showing slit-shaped breakouts, while low porosity rocks with high strength, such as granite, tend to form dog-ear shaped breakouts or tensile fractures. Anisotropy can also affect the shape and the orientation of breakouts, as discussed in (Choens et al., 2019), on the basis of experimental results on shale.

The micromechanics of failure also vary depending on the rock type and on the stress state. In sandstones under medium mean pressure shear failure or spalling was observed, while grain crushing was noted for slit-shaped breakouts (Haimson, 2007). Spalling and extensile failure seem to be the dominant mechanism in granitic rocks, as shown in (Lee & Haimson, 1993). For the modeling the micromechanical mechanism of failure is secondary and expressed in the failure criterion, but, for the understanding of the mechanical procedure underlying the formation and arrest of breakouts, the micromechanics are of great importance.

2.2 Breakout formation and arrest

As already mentioned, the geometry of the failure of the borehole wall varies strongly with the mode of failure. Tensile failure takes place when the tensile stresses at the borehole circumference are larger than the tensile strength of the rock. This happens when the ratio of the maximum to the minimum in-plane principal stress or the internal pressure

in the borehole are large enough. The failure presents itself in the form of a crack oriented parallel to the direction of the maximum in-plane principal stress, as shown after hydraulic fracturing tests on sandstone blocks (Stanchits, Surdi, & Gathogo, 2014). As a rule, such tensile cracks are not denoted as breakouts, but they belong in the same category from a physical and mechanical point of view.

Shear or splitting failure produces so called 'dog-ear' or 'cusp' breakouts, similar to what was observed on tests on a porous sandstone in (Haimson & Lee, 2004). It is mostly this type of borehole breakout that is used for the assessment of the *in situ* primary stress state. Compaction induced failure leads to slit shaped breakouts, very similar to compaction bands, and was also observed in tests on porous sandstone by (Haimson & Lee, 2004). Such breakouts are also in part induced by shear stresses, but close observation has shown fragmentation of grains at the advancing tip (Haimson & Lee, 2004), such as what is observed in compaction bands. This mode has only received more attention in the last years.

Failure may be ductile or brittle. In the first case the material response may be hardening or softening, but continuity is preserved. The damaged zone continues carrying some amount of load, even if not to the same extent as it did before yield. In the case of brittle failure continuity is lost. The damaged material is removed from the borehole wall, leaving a gap behind. In reality, the distinction is not perfectly clear cut. Closer observations using methods, such as scanning electron microscope imaging or thin sections, have shown damaged areas in the vicinity of the breakout (Haimson, 2007; Lee & Haimson, 1993) in cases where the general image was that of brittle failure. This indicates the likely presence of a process zone also in the case of what macroscopically appears to be brittle failure.

Scale effects are commonly present in rock mechanics. It has been observed that the initiation of breakout formation is strongly sensitive to scale. Boreholes, shafts or tunnels with large diameters start showing damage at loads that are in agreement with theoretical predictions using the solution of Kirsch. Smaller openings on the other hand only start exhibiting failure at much higher loads, often several times greater than the ones theoretically predicted by the theory of Kirsch (Cuss, Rutter, & Holloway, 2003; Meier et al., 2013). Based on elasticity theory, the initiation of breakouts should take place when the external pressure is equal to one half of the uniaxial strength. The external pressure at which breakout initiation is observed is known as critical pressure. As shown in Figure 5, breakout initiation is observed at significantly higher loads than those predicted by the elastic solution, depending on the material and on the size of the hole.

It has been observed by several authors, such as in (Herrick & Haimson, 1994; Zheng, Kemeny, & Cook, 1989), that the propagation of the breakouts takes place in such a way that their width remains constant, while the depth gradually increases. The procedure is sketched in Figure 2. Successive zones of material are detached either by spalling or by the formation of shear bands. Each successively detached domain is less wide than the

previous one, leading to an overall shape that becomes narrower with increasing depth. The procedure continues until the arrest of the failure propagation.

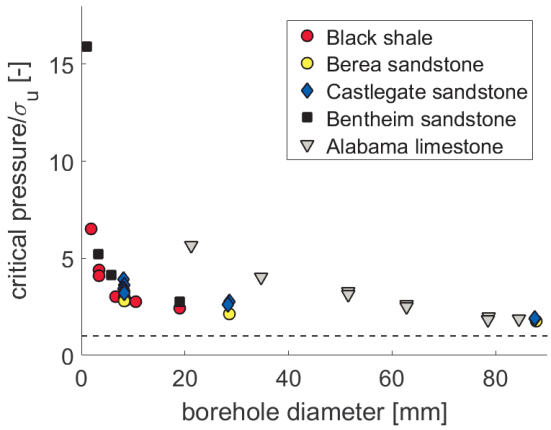

Figure 5. Scale effects as observed in laboratory tests.

The reasons for the arrest of dog-ear of cusp breakouts are not completely clear. The arrest may be purely linked to shape variations that lead in turn to stress redistribution. This is however not likely to be the only reason. It has been postulated that the phenomenon is linked to a plastic zone (Cheatham, 1993) or a process zone (Meier et al., 2013). The effect is the same as that of the formation of a plastic radius around a circular hole: the stresses are locally reduced, and the elastic domain is protected. Alternatively, the arrest has been attributed to scale effects, see for example (Herrick & Haimson, 1994), which may in turn be linked to the formation of a process zone.

2.3 Prediction and simulation

The material response can be ductile or brittle. The simulation of breakout formation is challenging in both cases, in the first case because of the softening of the material and in the second case because of the loss of continuity. In the ductile regime, failure is characterized by zones of localized deformation that cannot be modeled by simple constitutive models in the sense of Noll (Noll, 1972). Nonlocal (Crook, Willson, Jian, & Owen, 2003), micropolar (Papamichos, 2010) or higher gradient (Zervos, Papanastasiou, & Vardoulakis, 2001) models can be used to simulate the formation of breakouts in materials exhibiting softening. In the brittle regime both continuum and discrete numerical methods have been proposed to simulate borehole breakouts. Among others, (Herrick & Haimson, 1994; Zheng et al., 1989) used the boundary element method to

simulate the development of borehole breakouts in brittle rocks and recently (Zhang, Yin, & Aadnoy, 2018) proposed a methodology using the finite element method. Simulations using discrete elements have also attempted to provide an answer (H. Lee, Moon, & Haimson, 2016). In this case, the limited number of particles that can be used poses a limit to the applicability, since the size dependence that has been observed *in situ*, numerically and in the lab, plays a significant role. In terms of analytical methods, conformal mapping has been used in (Exadaktylos & Stavropoulou, 2002) to evaluate the stress field around underground openings. However, the shape of the opening has always been considered known and constant and the provided solutions are only valid for a specific form of the mapping.

2.4 Stress state assessment

As already mentioned, observations both in the laboratory and in the site have shown that breakouts evolve in depth, rather than in width, as shown in Figure 2. This means that successive spalling or shear fracture formation takes place, with the width of the breakout remaining constant and the depth gradually increasing.

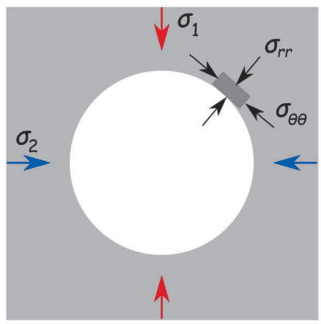

Figure 6. Radial and tangential stresses.

The width of the breakout is therefore determined by the failure of the initial circular shape of the borehole cross-section. For the initial, circular geometry analytical solutions are available, based on the theory of elasticity. The most commonly used one is the so-called solution of Kirsch, known also as the solution of Michell (Michell, 1899). Assuming the pressure of the drilling fluid to be equal to p_0, the solution provides the radial and tangential stresses at the borehole wall as illustrated in Figure 6:

$$\sigma_{rr} = p_0 \tag{1}$$

$$\sigma_{\theta\theta} = (\sigma_1 + \sigma_2) + 2\,(\sigma_1 - \sigma_2)\cos(2\theta) - p_0 \tag{2}$$

If the pressure of the drilling fluid is not present, the stress state at the borehole wall is uniaxial, meaning that the wall will fail, when the tangential stress is larger than the uniaxial strength σ_u. This leads to a linear relationship between the principal stresses:

$$\sigma_u = (\sigma_1 + \sigma_2) + 2\,(\sigma_1 - \sigma_2)\cos(2\theta) \tag{3}$$

where θ is the aperture angle of the breakout, as shown in Figure 3. If one of the two principal stresses is known, then the other stress can also be evaluated. If none of the two is known, additional information is required to estimate the value of each of the two stresses. In the present report, a numerical iterative approach is applied to make use of the breakout depth, as well as of the breakout width.

3. GENERAL METHODOLOGY

As already mentioned, two different problems are tackled. For the first, conformal mapping is used to simulate the progressive formation of breakouts, including their depth and precise shape. For the second, the known shape of the borehole breakout is used to determine the stress state. For both cases the underlying assumptions are similar and are discussed in the following section. The different parts of each of the algorithm are discussed in the last section of this chapter. The details of the algorithms used are described in detail in the corresponding chapters.

3.1 Assumptions

For the present analysis it is assumed that plane strain is a good approximation of the *in situ* conditions, that the material response is elastic-perfectly brittle and that the material surrounding the borehole is isotropic, as far as its elastic response is concerned. Anisotropy can be incorporated in solutions using the method of conformal mapping, but such methods were not used here.

3.2 Algorithm

Two algorithms were developed in the frame of this project. The first is used for the evaluation of the shape of the borehole breakouts, while the second is used for the evaluation of the *in situ* stress and uses the first algorithm as a subroutine.

The algorithm for the breakout evaluation is outlined in Figure 7. The initial borehole shape is assumed to be circular, though other shapes can also be handled by the code. The Michell solution (Michell, 1899) is used to evaluate the stress state around the circular borehole. Using the failure criterion, the area around the borehole where the material fails is marked and removed. The new boundary of the borehole is evaluated. (●) Conformal mapping is used to evaluate the stress state around the new geometry. The area that fails is again removed from the geometry and the new boundary is assessed. The procedure is repeated from (●) until the area that fails becomes smaller than the tolerance selected in the algorithm.

For the estimation of the *in situ* stress state, the previous algorithm is used as a subroutine and the depth and width of the breakout are used as input. The width of the breakouts is used to estimate a linear relationship between the principal stresses as explained in section 2.4. Two starting points are selected in terms of the minimum principal stress. From the Michell solution the maximum principal stress is evaluated for the two points and, using the first algorithm, the corresponding depth of the breakout is calculated. A modified bisection method is used to gain a new interval for the solution and the new stress state

and depth are evaluated. The algorithm is halted when the evaluated breakout depth is within tolerance from the target breakout depth. The tolerance is set by the user.

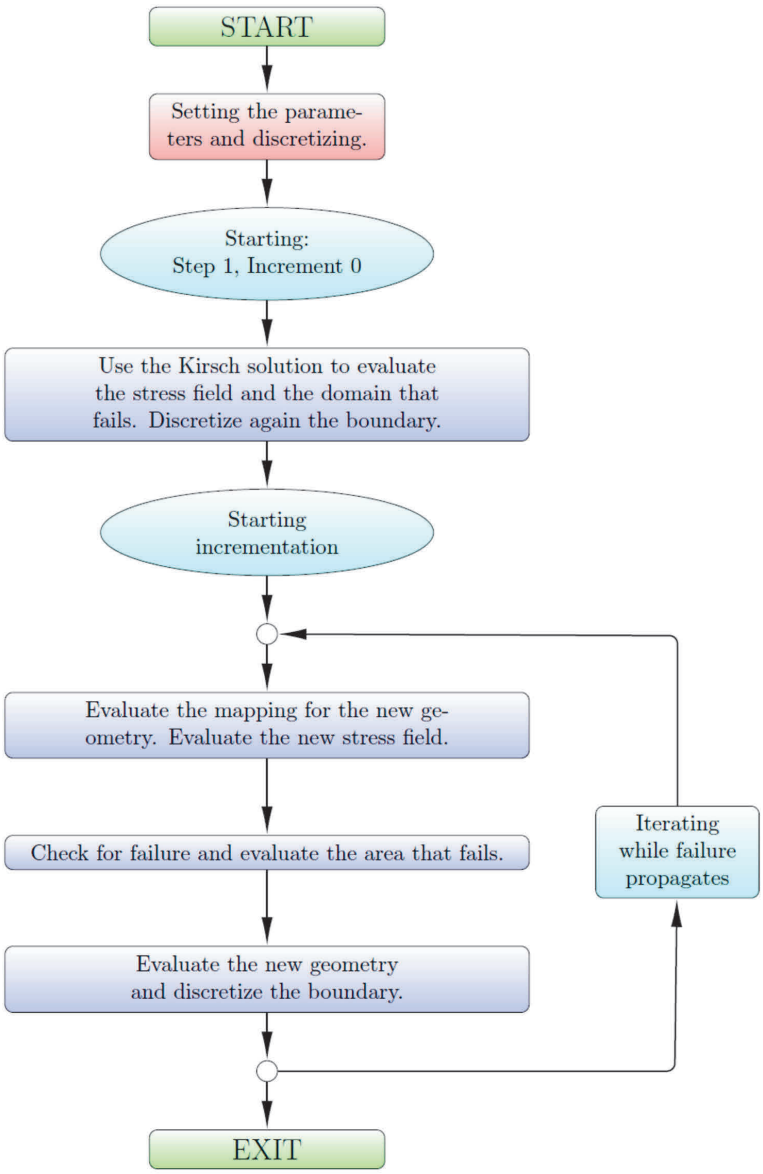

Figure 7. Outline of the algorithm for breakout shape evaluation.

3.3 A note on conformal mapping

For the present analysis conformal mapping is used. Since the method is not commonly used in applied geomechanics, a note is included here for the readers that do not wish to delve into depth in the underling mathematics, presented in the next chapter.

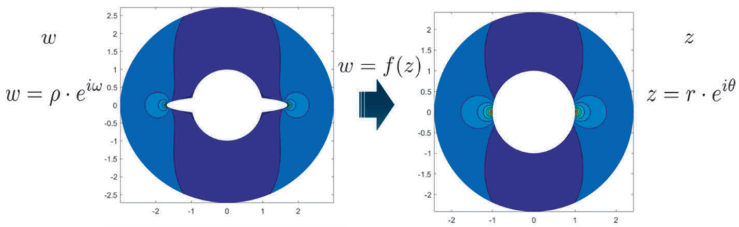

Figure 8. Mapping from a complicated domain with a simple boundary condition to a simple domain with a complicated boundary condition.

Conformal mapping aims to transform a problem with a complicated geometry into a problem with a simple geometry. The coordinates of the complicated geometry are a conformal map of the coordinates of the simple geometry. A conformal map is a transformation that preserves angles between two lines. In two dimensions this requirement is fulfilled by any complex function that is infinitely differentiable. The main property is that the solution of the Laplace equation on the original domain will be a solution of the Laplace equation in the mapped domain. When other equations than the Laplace need to be solved, such as the stress balance equations, the solution becomes more difficult and requires an adaptation of the boundary conditions, as shown in Figure 8.

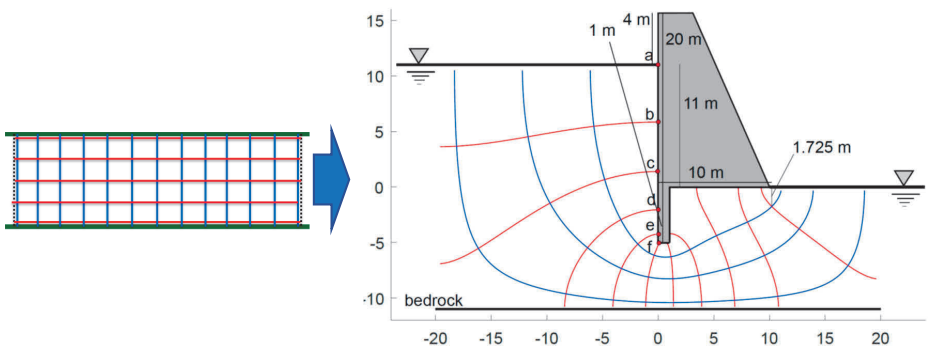

Figure 9. Conformal mapping applied to water flow.

Common areas of application of conformal mapping may be found in (Schinzinger & Laura, 2003), but briefly stated they include electromagnetism, stationary and non-stationary flows and airfoils. In geomechanics the most common domain of application are flow nets, where conformal mapping is used to evaluate the isopressure lines and the flow lines. An example is shown in Figure 9.

4. CONFORMAL MAPPING

Here conformal mapping is used to simulate the progressive formation of breakouts, including their depth and precise shape. The algorithm and the basic underlying theory are given in the rest of the present chapter. The details of the implementation, as well as the validation against known solutions are also presented.

4.1 Underlying theory

Here the application of conformal mapping to elastic solids is summarized. A more extended introduction to the topic may be found in (Muskhelishvili, 2010; Schinzinger & Laura, 2003). It is well known from the theory of elasticity that the stresses in a planar elastic medium can be written as

$$\sigma_{xx} = \frac{\partial^2 U}{\partial y^2}, \quad \sigma_{yy} = \frac{\partial^2 U}{\partial x^2}, \quad \sigma_{xy} = -\frac{\partial^2 U}{\partial x \partial y} \tag{4}$$

where $U(x, y)$ is an appropriate solution of the biharmonic equation. The solution may be expressed in terms of analytic functions as

$$U(z) = \Re[\bar{z}\phi(z) + \chi(z)] \tag{5}$$

This means that the stresses can be expressed as

$$\sigma_{xx} + \sigma_{yy} = 4Re[\phi'(z)] = 4\Re[\Phi(z)] \tag{6}$$

$$\sigma_{yy} - \sigma_{xx} + 2i\sigma_{xy} = 2[\bar{z}\phi''(z) + \chi'(z)] = 2[\bar{z}\Phi'(z) + X(z)] \tag{7}$$

$$\sigma_{\theta\theta} - \sigma_{rr} + 2i\sigma_{r\theta} = [\sigma_{yy} - \sigma_{xx} + 2i\sigma_{xy}]e^{2i\theta} \tag{8}$$

where

$$\Phi(z) = \phi'(z), \quad X(z) = \chi'(z) \tag{9}$$

For the boundary condition along the boundary $\mathcal{L}$ in terms of tractions, one possible form is

$$\sigma - i\tau = 2\Re[\Phi(z)] - e^{2i\alpha}[\bar{z}\Phi'(z) + X(z)] \tag{10}$$

where σ and τ are the normal and the tangential components of the external stresses acting on the boundary $\mathcal{L}$, or, more specifically, the projections of the stresses on the outward normal $\mathbf{n}$ and on the tangent $\mathbf{t}$, pointing to the left of $\mathbf{n}$. α is the angle between the normal $\mathbf{n}$ and the axis Ox, measured from the latter. Another possible form of the boundary condition reads

$$i\int_{\mathcal{L}} (f_x + if_y)ds = \phi(z) + z\overline{\phi'(z)} + \overline{\chi(z)} \tag{11}$$

The solution of the above problem is relatively straightforward when the geometry of the opening can be easily described analytically, for example for circular or slit shaped

openings. As the geometry becomes more complicated, the boundary conditions become increasingly difficult to handle. To resolve the issue, conformal mapping is used. The idea is to transform a relatively simple problem with a complicated geometry into a more complicated problem with a simple geometry. The domain in which the solution is sought may be called the actual domain and symbolized as w, while the domain with the simplified geometry used to solve the problem may be called the reference domain and symbolized as z. A conformal map between the two domains exist, with certain properties, such as angle preservations, as shown in Figure 10. A conformal map is a function mapping a geometry to another one while preserving orientation and angles among curves locally, meaning for example that equipotential lines and flow lines remain normal to each other after the projection.

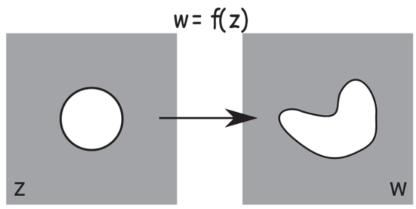

Figure 10. Mapping from the reference to the actual domain.

It is assumed that the following conformal maps are known

$$z = \omega(w) \tag{12}$$

$$w = f(z) \tag{13}$$

Let us denote by

$$\phi_1(z), \quad \chi_1(z), \quad \Phi_1(z), \quad X_1(z) \tag{14}$$

the functions written earlier as

$$\phi(z), \quad \chi(z), \quad \Phi(z), \quad X(z) \tag{15}$$

and introduce the new notation

$$\phi(w) = \phi_1(z) = \phi_1(\omega(w)), \quad \chi(w) = \chi_1(z) = \chi_1(\omega(w)) \tag{16}$$

Expressing the solution in the w-domain in terms of the solution in the z-domain yields

$$\sigma_{xx} + \sigma_{yy} = 4Re[\phi'(w)] = 4\Re\left[\phi_1'(z)\frac{\mathrm{d}z}{\mathrm{d}w}\right] = 4\Re\left[\frac{\phi_1'(z)}{f'(z)}\right] \tag{17}$$

$$\sigma_{yy} - \sigma_{xx} + 2i\sigma_{xy} = 2[\bar{w}\phi''(w) + \chi'(w)] \Rightarrow \tag{18}$$

$$\sigma_{yy} - \sigma_{xx} + 2i\sigma_{xy} = 2\left[\bar{w}\frac{\phi_1''(z)f'(z) - \phi_1'(z)f''(z)}{f'(z)^3} + \frac{\chi_1'(z)}{f'(z)}\right] \tag{19}$$

$$\sigma_{\theta\theta} - \sigma_{rr} + 2i\sigma_{r\theta} = [\sigma_{yy} - \sigma_{xx} + 2i\sigma_{xy}]e^{2i\theta} \tag{20}$$

The boundary condition that needs to be satisfied then reads

$$\phi_1(z) + \frac{f(z)}{\overline{f'(z)}}\overline{\phi_1'(z)} + \overline{\chi_1(z)} = i\int \left(f_x + if_y\right)ds \tag{21}$$

4.2 Evaluation of the conformal map

Since the aim is to model the evolving geometry of boreholes, it is reasonable to select an infinite plate with an opening in the form of the unit circle as the reference domain. Accordingly, the solution is mapped from the exterior of a borehole with breakouts to the exterior of the circle. z is the domain expressing the exterior of the circle and w is the domain in which the solution is sought. It is known that w can often be expressed as a series expansion with respect to z with the form

$$w = \sum_{n=0}^{\infty} q_n z^{1-n} \tag{22}$$

or

$$w = Rz + \sum_{n=1}^{\infty} q_n z^{-n} \tag{23}$$

here, for the last equation, it is possible to retain only the double exponents, since the geometry is expected to be symmetric, both with respect to the vertical and the horizontal axis. For the sake of generality, all terms are retained in this work.

It should be noted that equation (23) is not truly equivalent to equation (22). Two assumptions have been made. The first is that the constant term in the series expansion of equation (22) is equal to zero. As this term only expresses a displacement, there is no loss in generality in making this assumption. The other assumption that has been tacitly made is that the imaginary part of the first term is equal to zero. The imaginary part of that term corresponds to a rigid rotation. The term can as a result be only ignored when one of the symmetry axes of the actual domain corresponds to the horizontal or to vertical axis in the reference domain. As there is no loss in generality in assuming that the principal stresses are horizontal and vertical respectively, the assumption that the coefficient of the first term of the series is a real number is made here.

The mapping should map the unit circle $|z| = 1$ on the desired boundary in the w-space. It is assumed that

$$z = r \cdot e^{i\theta}, \quad w = \rho \cdot e^{i\omega} \tag{24}$$

where it should be noted that the arguments θ and ω do not necessarily coincide.

We will use here a variant of the method of simultaneous equations, introduced by Kantorovich (Kantorovich, 1933). The variation is introduced, because we wish to map the exterior of the actual geometry to the exterior of the unit circle, rather than considering the interiors. The actual boundary can theoretically be expressed as a real function of the angle θ and the same holds for its square. Thus, the curve of the boundary can be expressed as

$$w \cdot \bar{w} - R(\omega)^2 = w \cdot \bar{w} - F(\theta) = 0 \tag{25}$$

The function $F(\theta)$ can be expressed on approximation as a truncated Fourier series of the form

$$F(\theta) = \sum_{n=-k}^{k} c_n e^{in\theta} \tag{26}$$

either using a Fast Fourier Transform or a least squares approximation. It should be noted that while the function $R(\omega)$ is known, the same is not true of the function $F(\theta)$. The relationship between the arguments θ and ω is not known, which in turn means that the coefficients c_n are not known.

An approximate mapping of the form

$$w = \sum_{n=0}^{k} q_n z^{1-n} \tag{27}$$

is sought. The boundary corresponds to the unit circle in the reference domain, meaning that on the boundary

$$z = e^{i(1-n)\theta} \tag{28}$$

which in turn means that for the boundary the mapping reads

$$w|_{\mathcal{L}} = \sum_{n=0}^{k} q_n e^{i(1-n)\theta} \tag{29}$$

Introducing the above in equation (25), one gets

$$\sum_{n=0}^{k} q_n e^{i(1-n)\theta} \sum_{m=0}^{k} \bar{q}_m e^{i(m-1)\theta} = \sum_{n=-k}^{k} c_n e^{in\theta} \Rightarrow \tag{30}$$

$$\sum_{n=0}^{k} \sum_{m=0}^{k} q_n e^{i(1-n)\theta} \bar{q}_m e^{i(m-1)\theta} = \sum_{n=-k}^{k} c_n e^{in\theta} \Rightarrow \tag{31}$$

$$\sum_{n=0}^{k} \sum_{m=0}^{k} q_n \bar{q}_m e^{i(m-n)\theta} = \sum_{n=-k}^{k} c_n e^{in\theta} \Rightarrow \tag{32}$$

$$\sum_{u=0}^{k}\sum_{m=u}^{k} q_{m-u}\bar{q}_m e^{iu\theta} + \sum_{u=0}^{k}\sum_{n=u}^{k} q_n\bar{q}_{n-u} e^{-iu\theta} = \sum_{n=0}^{k} c_n e^{in\theta} + \sum_{n=1}^{k} \bar{c}_n e^{-in\theta} \tag{33}$$

$$\sum_{n=0}^{k}\sum_{m=n}^{k} q_{m-n}\bar{q}_m e^{in\theta} + \sum_{n=0}^{k}\sum_{m=n}^{k} q_m\bar{q}_{m-n} e^{-in\theta} = \sum_{n=0}^{k} c_n e^{in\theta} + \sum_{n=1}^{k} \bar{c}_n e^{-in\theta} \tag{34}$$

Equating the terms with the same exponents, yields the following system of k+1 equations, with $n \in \{0, 1, \ldots, k\}$.

$$\sum_{m=n}^{k} q_{m-n}\bar{q}_m = c_n \tag{35}$$

Assuming the complex coefficients to be of the form

$$q_m = p_m + is_m \tag{36}$$

where p_m and s_m are real numbers, the above product may be written as

$$\sum_{m=n}^{k} (p_{m-n} + is_{m-n})(p_m - is_m) = c_n \Rightarrow \tag{37}$$

$$\sum_{m=n}^{k} (p_{m-n}p_m + s_{m-n}s_m) + i(s_{m-n}p_m - s_m p_{m-n}) = c_n \Rightarrow \tag{38}$$

$$\begin{aligned} \textstyle\sum_{m=n}^{k} (p_{m-n}p_m + s_{m-n}s_m) &= \Re c_n \\ \textstyle\sum_{m=n}^{k} (s_{m-n}p_m - s_m p_{m-n}) &= \Im c_n \end{aligned} \tag{39}$$

This method can be applied, when the function $F(\theta)$ is known, which is generally not the case. To circumvent the problem, a procedure similar to the one suggested by Fornberg (Fornberg, 1980) is used here. The N-roots of unity in the z-space are used for the series expansion, where N is the discretization selected on the boundary. For the first iteration, it is assumed that the arguments correspond with the ones of the corresponding points in the w-space, meaning that the following assumption is made

$$\theta_i = \omega_i^{(1)} \tag{40}$$

meaning in turn that implicitly the following assumption is made:

$$F(\theta) = R^2(\theta) \tag{41}$$

see also equation (25). In the above equations the superscript stands for the number of iterations.

Then, the method suggested by Kantorovich (Kantorovich, 1933) with the modifications suggested here is used and an approximate mapping is evaluated

$$w^{(1)}\big|_{\mathcal{L}} = \sum_{n=0}^{k} q_n^{(1)} e^{i(1-n)\theta} \tag{42}$$

The arguments of the points in the w-space are assessed again and the values of the function $F(\theta)$ are evaluated again. The procedure is repeated, until a satisfactory fit is achieved.

It is obvious from the above that the coefficients q_n of the series need to be evaluated at each iteration. For their evaluation the system of equation (39) needs to be solved. To this end the Newton-Raphson method is used. It was observed that large increments in the coefficients lead to large changes in the arguments, which in turn leads to failure to converge. To alleviate the problem a relaxation parameter is used for the incrementation

$$q_n^{(k),m} = q_n^{(k),m-1} - \zeta u^k \tag{43}$$

where m is the increment number of the Newton-Raphson, u is its increment and ζ is the relaxation parameter.

4.3 Alternative formulation

As an alternative the method suggested by Fornberg is tested (Fornberg, 1980). As this method was created to map the interior of the unit circle to the interior of the desired domain, certain modifications are necessary in the present case, where external domains are considered. This modified version is described here, with little reference to the original method. Let z_k, $k = 1, \ldots, N$ be the N roots of unity. A discrete Fourier transform (DFT) yields a mapping

$$w(z_k) = \sum_{\nu=-N/2+1}^{N/2} d_\nu z_k^\nu \tag{44}$$

from the unit circle on the desired boundary. This function fails to converge at infinity, due to the terms with $\nu > 1$. The goal is to move the points w_k along the boundary, so that the function w(z) becomes a suitable mapping, or, in other words, so that

$$d_\nu = 0 \text{ for } \nu = 2, \ldots, N/2 \tag{45}$$

The remaining coefficients will yield the desired mapping of the form

$$w(z) = \sum_{\nu=-1}^{N/2-1} q_\nu z^{-\nu} \tag{46}$$

The suggested approach consists of inner and outer iterations. The outer iteration is described first.

The boundary curve $\mathcal{L}$ is assumed to be smooth, simply connected and enclosing the origin in a complex plane. Since $\mathcal{L}$ is smooth, the true mapping function w(z) can be represented by a convergent Taylor series as

$$w(z) = \sum_{\nu=-1}^{\infty} q_\nu z^{-\nu} \tag{47}$$

The following form for the approximate mapping will be used

$$\zeta(z) = \sum_{\nu=-1}^{N/2-1} d_\nu z^{-\nu} \tag{48}$$

so that the points ζ_k lie monotonically along $\mathcal{L}$ and represent guesses for the numbers w_k. The above equation can also be written as

$$\zeta_k = \sum_{\nu=-1}^{N/2-1} d_\nu \omega^{-k\nu} \tag{49}$$

with $\omega = \exp(2\pi i/N)$.

The coefficients d_ν can be evaluated using the inverse DFT:

$$d_\nu = \frac{1}{N} \sum_{k=0}^{N-1} \zeta_k \omega^{-k\nu}, \quad \nu = -\frac{N}{2} + 1, \ldots, \frac{N}{2} \tag{50}$$

We wish to move these points ζ_k on $\mathcal{L}$ in such a way that d_ν becomes equal to zero for $\nu = 2, \ldots, N/2 - 1$. With N free real parameters, we wish to make N/2-1 complex numbers zero. This count of equations and unknowns appears correct, but we have not yet prescribed a position to one of the points. It will transpire that the N equations obtained after linearization will form a system with rank only N-1 (to within truncation errors). We move the points ζ_k in a two-step process. Given the tangential directions e_k (with $|e_k| = 1$) at the points ζ_k on $\mathcal{L}$, we can try to move these points in the tangential directions by distances t_k, in such a way that $d_\nu, \quad \nu = 2, \ldots, N/2$ become zero:

$$0 = \frac{1}{N} \sum_{k=0}^{N-1} (\zeta_k + t_k e_k) \omega^{-k\nu}, \quad \nu = 2, \ldots, \frac{N}{2} \tag{51}$$

Afterwards, the points $\zeta_k + t_k e_k$ are moved back to the curve $\mathcal{L}$.

By subtracting the last two equations, we get N/2-1 complex linear equations for the N real unknowns t_k:

$$d_\nu = -\frac{1}{N} \sum_{k=0}^{N-1} t_k e_k \omega^{-k\nu}, \quad \nu = 2, \ldots, \frac{N}{2} \tag{52}$$

Dividing the real and the complex parts of the above linear equations yields N-2 equations. Setting t_0=0 reduces the number of unknowns to N-1. We are still one equation short. One option is to set the imaginary part of d_1 to zero.

Fornberg (Fornberg, 1980) suggests a conjugate gradient method to solve the above system of equations. Assuming that the tangents e_k are known, it would however be possible to solve the linear system for t_k after separating the real and the imaginary parts.

Since for the points on the curve the approximation ζ is used, for the tangent the approximation ζ' will be used.

Once the real quantities t_k have been evaluated the new points ζ_k on the curve are evaluated.

4.4 Comparison of the two methods

Both methods have been programmed and used on a variety of shapes. It was found that the method suggested by Fornberg and based of the Fast Fourier Transform is significantly faster than the method suggested by Kantorovich. The times required by the Fornberg method were in most cases less than half of the time required by the Kantorovich method.

On the other hand, the Kantorovich method proved to be much more stable. Even though it is stated in the original publication that the method will converge only for shapes that are very close to the circle, it was found that this was rather the case for the Fornberg method. The method of Kantorovich succeeded in converging to the correct shape over a much wider variety of shapes and for significantly greater deviations from the circular shape.

4.5 Examples using the method of Kantorovich

To begin with an example of the procedure of convergence is given. A target shape similar to that of a borehole with breakouts was chosen and different iterations of the mapping algorithm were sketched as shown in Figure 11.

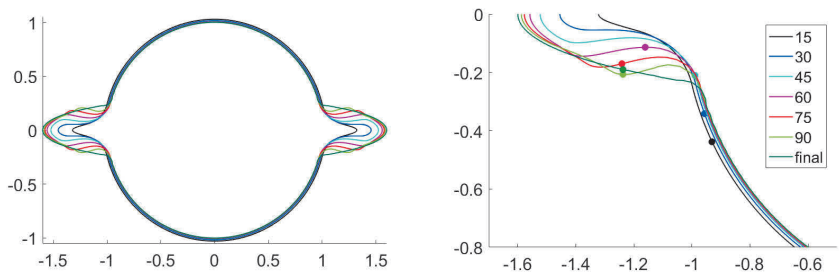

Figure 11. Left: iterations of the mapping algorithm and convergence to the final shape. Right: visualization of the migration of a single point during iterations and change in the argument.

The total number of iterations was smaller than 150 and the mapping of the target shape was achieved with great accuracy. The relaxation parameter was selected equal to 0.02. This is a small value, a fact that is often necessary for narrow and deep breakouts. On the left of Figure 11 the result of the mapping at different iterations is shown. The different lines correspond to the number of iterations given in the legend of the subfigure on the right. The gradual convergence to the final shape is easy to observe.

For the right subfigure an argument was selected in the reference domain and maintained constant. The corresponding point in the actual domain is plotted in the figure for the different iterations. It can be easily observed that the argument in the actual domain varies according to the mapping and is not necessarily equal to the argument in the reference domain. This fact renders the successive approximations in the mapping algorithm as well as the relaxation parameter necessary.

To assess the effectiveness of the code, three different shapes where mapped at different discretizations. The aim is to illustrate the suitability of the code to map different shapes. To this end shapes were used that are common in tunneling or for borehole breakouts. The first is a horse-shoe shaped tunnel, while the other two represent boreholes with dog-ear shaped and slit-shaped breakouts respectively. The parameters α and β are used to describe the shape and their meaning for each shape is illustrated in Figure 12.

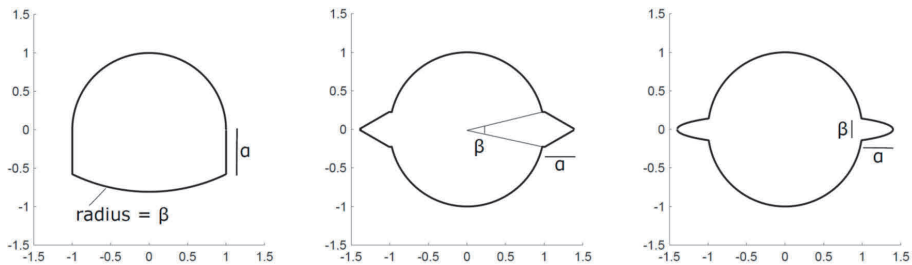

Figure 12. Different shapes used for the verification of the effectiveness of the mapping algorithm. Left: Horse-shoe tunnel. Middle: Dog-ear breakout. Right: Slit-shaped breakout.

Circular segments for which the radius is not given have a radius equal to one. The precision for the series coefficients was set to 10^{-8}, while the error was defined as the mean deviation of the resulting curve from the original one. Some results are presented in Table 1, where k stands for the number of terms in the series approximation, n for the number of points on the curve and ζ for the relaxation factor used. The last shape was found to be the most challenging to fit. The time was measured on a personal computer on single runs of the code and should therefore be viewed as indicative.

Some examples are shown in Figure 13. As seen on the left of Figure 13 the quality of the fit improves with increasing number of series terms, especially where the shape has angles. As would be expected, the time necessary for the fit increases with increasing number of terms and increasing number of input point for the curve. A larger value of ζ leads to faster convergence but decreases the likelihood for the solution to be reached. This is especially the case for shapes such as the second and third shape considered here, which deviate from the circle in a more pronounced manner.

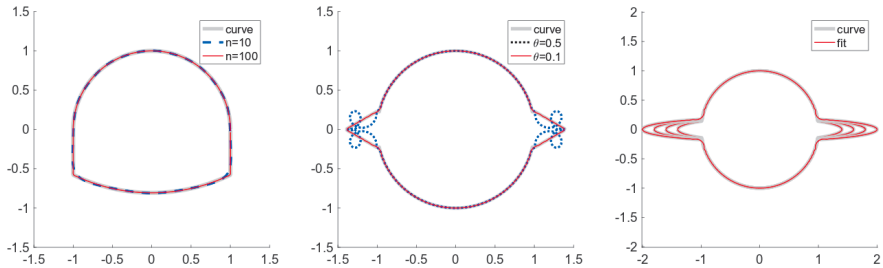

Figure 13. Shape fitting with the Kantorovich method. Left: Horse-shoe tunnel. Middle: Dog-ear breakout. Right: Slit-shaped breakout.

In fact, the second shape fails to converge with a value of ζ equal to 0.5, but converges when ζ is set to 0.1, at an additional cost in terms of time. As may be seen in the middle of Figure 13, the failure to converge is a result of argument miscalculation. Examples for a borehole with slit-shaped breakouts are shown on the right of Figure 13 for increasing depths of the breakout. The fit remains satisfactory but requires a small value of ζ and therefore also a larger number of iterations and longer times to converge. It would be possible to reduce the time required to calculate the mappings for such shapes, which deviate strongly from the circle, by varying ζ, selecting a small value for the first iterations and increasing values for the subsequent ones. This was not attempted here.

Table 1. Conformal map evaluation for different shapes.

Geometry	α	β	n	k	ζ	Iter.	Error	Time [sec]
1	0.5	2.3	512	10	0.5	10	1.6e−04	0.58
1	0.5	2.3	1024	10	0.5	9	1.14e−04	1.42
1	0.5	2.3	512	100	0.5	12	2.00e−06	0.87
2	0.4	π/6	1024	10	0.5	2	1.3e−03	0.57
2	0.4	π/6	1024	100	0.5	max	1.3e−03	24.19
2	0.4	π/6	1024	100	0.1	53	4.2629e−05	1.77
3	0.4	0.2	1024	100	0.02	281	8.8359e−05	7.79

3	0.4	0.2	1024	100	0.01	516	8.8260e−05	13.30
3	0.4	0.2	1024	200	0.01	275	4.1508e−05	17.81
3	0.6	0.2	1024	200	0.01	324	6.4821e−05	20.74
3	0.8	0.2	1024	200	0.01	384	7.2559e−05	24.47
3	1.0	0.4	1024	200	0.01	468	8.8358e−05	29.06

On the whole, the algorithm for the evaluation of the conformal maps performs satisfactorily, even for shapes that deviate significantly from the circle, as shown in Figure 13, where the maximum depth of the slit-shaped breakout is equal to the radius of the borehole.

4.6 Theory for the stress state estimation

For the evaluation of the stress state the functions $\phi_1(z)$ and $\chi_1(z)$ need to be evaluated, as discussed in section 4.1. It is reminded that these functions are defined in the reference rather than in the actual domain. In the z domain the solution is of the form

$$\phi_1(z) = Az + \sum_{n=1}^{\infty} A_n z^{1-n} \tag{53}$$

and

$$\chi_1(z) = Bz + \sum_{n=1}^{\infty} B_n z^{1-n} \tag{54}$$

The first derivatives of the above functions read

$$\phi_1'(z) = A + \sum_{n=1}^{\infty} (1-n) A_n z^{-n} = A + \sum_{n=1}^{\infty} a_n z^{-n} \tag{55}$$

and

$$\chi_1'(z) = B + \sum_{n=1}^{\infty} (1-n) B_n z^{-n} = B + \sum_{n=1}^{\infty} b_n z^{-n} \tag{56}$$

respectively.

From the boundary condition at infinity, where the stress state should be equal to the primary *in situ* stress state, it results that

$$A = \frac{\sigma_v + \sigma_h}{4} R \tag{57}$$

and

$$B = \frac{\sigma_v - \sigma_h}{2} R \tag{58}$$

where R is the first term of the conformal map, which does not necessarily coincide with the borehole radius for boreholes with breakouts. σ_v is the vertical in plane stress and σ_h is the horizontal in plane stress. This refers to the image representation in this report.

The constant terms in the series expansions are ignored, as they do not contribute to the stresses.

The boundary condition at the circle boundary can be derived from the expression

$$\sigma_{rr}-i\sigma_{r\theta}=\frac{\phi_1'(z)}{f'(z)}+\frac{\phi_1'(\bar{z})}{f'(\bar{z})}-\frac{z^2}{\rho^2 f'(\bar{z})}\left(f(\bar{z})\frac{\phi_1''(z)f'(z)-\phi_1'(z)f''(z)}{f'(z)^2}+\chi_1'(z)\right) \tag{59}$$

after (Muskhelishvili, 2010) , pp. 193-194.

Alternatively, the following holds

$$\phi_1(z)+\frac{f(z)}{\overline{f'(z)}}\overline{\phi_1'(z)}+\overline{\chi_1(z)}=i\int\left(f_x+if_y\right)\mathrm{d}s \tag{60}$$

In the case of an internal cavity under uniform pressure this yields

$$\phi_1(z)+\frac{f(z)}{\overline{f'(z)}}\overline{\phi_1'(z)}+\overline{\chi_1(z)}=p_0 w=p_0 f(z)\Rightarrow \tag{61}$$

$$\overline{f'(z)}\phi_1(z)+f(z)\overline{\phi_1'(z)}+\overline{f'(z)\chi_1(z)}-p_0 f(z)\overline{f'(z)}=0 \tag{62}$$

4.7 Least squares approximation for the stress state estimation

For the evaluation of the coefficients of the functions, two options are available. One possibility is to formulate each of the terms as one power series and then equate the terms of the same order. This strategy means that the solution will be valid at any point on the boundary. Particular difficulties are posed however by the positive and negative powers, which indicate that special treatment is necessary for conjugates.

Another option is to assume a discretization of the boundary and to demand equation (62) to hold on any point of that discretization. The linear system to be solved will then be over-constrained and the solution returned will be the answer to the corresponding least squares problem. This method is more straightforward and was examined first.

Let us consider s points z_j, $j=1,\ldots,s$ on the boundary. The quantities $f(z_j)$, $f'(z_j)$ and z_j^n for any are known. The solution is reduced to the linear system

$$\mathbf{C}\cdot\mathbf{x}=\mathbf{D} \tag{63}$$

where

$$x_n=\begin{cases}A_{1+n}, & n\in[1,k-1]\\ B_{2+n-k}, & n\in[k,2k-2]\end{cases} \tag{64}$$

$$D_j=-p_0 f(z_j)f'(\bar{z}_j)-A_0(f'(\bar{z}_j)z_j+f(z_j))-B_0\bar{z}_j f'(\bar{z}_j) \tag{65}$$

$$C_{j,n} = \begin{cases} z_j^{-n} f'(z_j) - n \cdot z_j^{-n-1} f(z_j), & n \in [1, k-1] \\ f'(z_j) \bar{z}_j^{k-1-n}, & n \in [k, 2k-2] \end{cases} \tag{66}$$

To test the implementation, the solution for a crack with half width 1 was compared against the corresponding analytical solution after (Kachanov, 1994). The external boundary is unloaded and the interior of the crack is subjected to a uniform pressure of measure 1. The conformal map should read

$$w = \frac{1}{2}\left(z + \frac{1}{z}\right) \tag{67}$$

and is assumed known in this case, so that all possible errors arise with certainty from the algorithm for the evaluation of the stress state. The stresses are given in Figure 14. The filled graph corresponds to the analytical solution for the crack, while the red lines give the corresponding isolines of the numerical solution. The top row shows the results for 16 and the bottom row for 26 interpolation terms. Subfigures (a) and (d) show σ_{xx}, subfigures (b) and (e) show σ_{xy} and subfigures (c) and (f) show σ_{yy}.

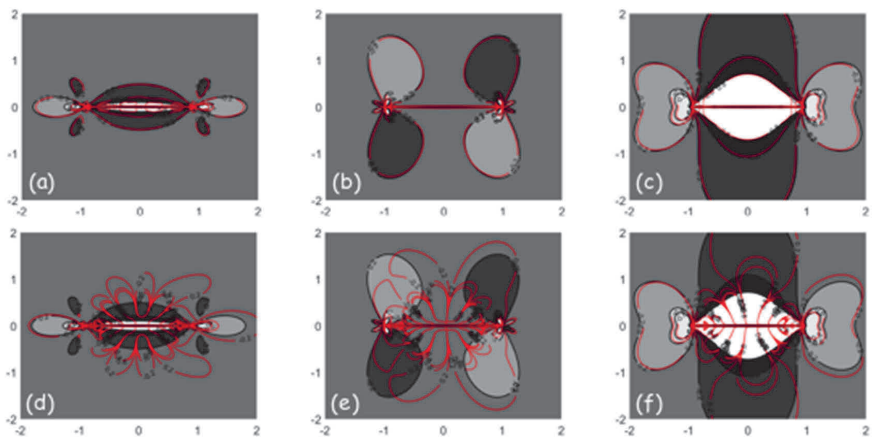

Figure 14. Results of the least squares approximation for a crack. The filled graph corresponds to the analytical solution for the crack, while the red lines give the corresponding isolines of the numerical solution.

The results of the top row, corresponding to the solution with 16 series terms, do not exactly coincide with the analytical solution, but are rather close to it. The results of the bottom row on the other hand show a large quantity of oscillations and are much further from the analytical solution than the interpolation with 16 terms. The same phenomenon is observed in Figure 15, where the values of the series coefficients are plotted for the same two cases. The approximation using less terms shows a regular response with the

coefficients of higher order terms mostly decreasing. The approximation using 26 terms on the other hand shows scattering which becomes more significant as the order of the terms increases. This indicates that the minimum recovered with a least squares approximation is not necessarily unique and does not need to correspond to the actual solution. In view of this the semi-analytical approach is examined next.

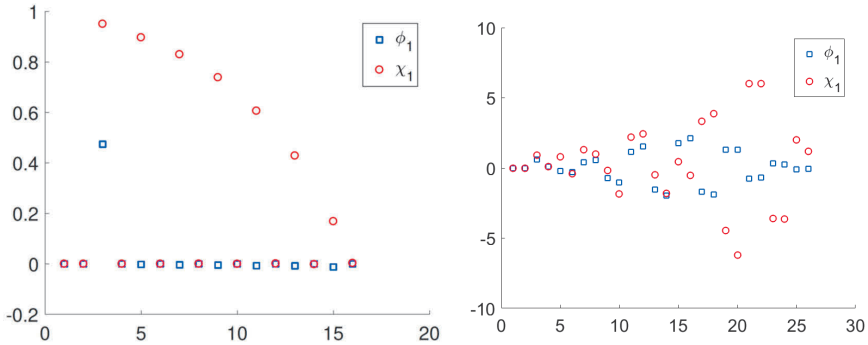

Figure 15. Series coefficients for the functions ϕ_1 and χ_1. Left: for 16 terms. Right: For 26 terms.

4.8 Semi-analytical method for the stress state estimation

In the equation expressing the boundary condition, equation (62), each of the terms will be expressed as a power series in what follows. Use will be made of the fact that

$$z = e^{i\theta} \tag{68}$$

since we are referring to the unit circle. The coefficients of the mapping are known, as are the first coefficients of the functions ϕ_1 and χ_1. Make use of the power series and the boundary condition it results that

$$\overline{f'(z)}\phi_1(z) + f(z)\overline{\phi_1'(z)} + \overline{f'(z)\chi_1(z)} - p_0 f(z)\overline{f'(z)} = 0 \Rightarrow \tag{69}$$

$$\begin{aligned} & \overline{f'(z)}\phi_1(z) \\ + \; & f(z)\overline{\phi_1'(z)} \\ + \; & \overline{f'(z)\chi_1(z)} \\ - \; & p_0 f(z)\overline{f'(z)} \\ = \; & 0 \Rightarrow \end{aligned} \tag{70}$$

$$
\begin{aligned}
& \sum_{n=0}^{k} A_n z^{1-n} \sum_{m=0}^{k} (1-m)\bar{q}_m \bar{z}^{-m} \\
+ & \sum_{n=0}^{k} (1-n)\bar{A}_n \bar{z}^{-n} \sum_{m=0}^{k} q_m z^{1-m} \\
+ & \sum_{n=0}^{k} \bar{B}_n \bar{z}^{1-n} \sum_{m=0}^{k} (1-m)\bar{q}_m \bar{z}^{-m} \\
- & p_0 \sum_{n=0}^{k} q_n z^{1-n} \sum_{m=0}^{k} (1-m)\bar{q}_m \bar{z}^{-m} \\
= & \; 0 \Rightarrow
\end{aligned}
\tag{71}
$$

$$
\begin{aligned}
& \sum_{n=0}^{k} \sum_{m=0}^{k} (1-m) A_n \bar{q}_m z^{1-n} \bar{z}^{-m} \\
+ & \sum_{n=0}^{k} \sum_{m=0}^{k} (1-n)\bar{A}_n q_m \bar{z}^{-n} z^{1-m} \\
+ & \sum_{n=0}^{k} \sum_{m=0}^{k} (1-m)\bar{B}_n \bar{q}_m \bar{z}^{1-n} \bar{z}^{-m} \\
= & \; p_0 \sum_{n=0}^{k} \sum_{m=0}^{k} (1-m) q_n \bar{q}_m z^{1-n} \bar{z}^{-m} \Rightarrow
\end{aligned}
\tag{72}
$$

$$
\begin{aligned}
& \sum_{n=2}^{k} \sum_{m=0}^{k} (1-m) A_n \bar{q}_m z^{1-n} \bar{z}^{-m} + \sum_{m=0}^{k} (1-m) A_0 \bar{q}_m z \bar{z}^{-m} \\
+ & \sum_{n=2}^{k} \sum_{m=0}^{k} (1-n)\bar{A}_n q_m \bar{z}^{-n} z^{1-m} + \sum_{m=0}^{k} \bar{A}_0 q_m z^{1-m} \\
+ & \sum_{n=2}^{k} \sum_{m=0}^{k} (1-m)\bar{B}_n \bar{q}_m \bar{z}^{1-n} \bar{z}^{-m} + \sum_{m=0}^{k} (1-m)\bar{B}_0 \bar{q}_m \bar{z} \bar{z}^{-m} \\
= & \; p_0 \sum_{n=0}^{k} \sum_{m=0}^{k} (1-m) q_n \bar{q}_m z^{1-n} \bar{z}^{-m} \Rightarrow
\end{aligned}
\tag{73}
$$

$$\begin{aligned}
&\sum_{n=2}^{k}\sum_{m=0}^{k}(1-m)A_n\bar{q}_m e^{i(1-n+m)\theta}+\sum_{m=0}^{k}(1-m)A_0\bar{q}_m e^{i(1+m)\theta}\\
+&\sum_{n=2}^{k}\sum_{m=0}^{k}(1-n)\bar{A}_n q_m e^{i(1-m+n)\theta}+\sum_{m=0}^{k}\bar{A}_0 q_m e^{i(1-m)\theta}\\
+&\sum_{n=2}^{k}\sum_{m=0}^{k}(1-m)\bar{B}_n\bar{q}_m e^{i(m+n-1)\theta}+\sum_{m=0}^{k}(1-m)\bar{B}_0\bar{q}_m e^{i(-1+m)\theta}\\
=&\ p_0\sum_{n=0}^{k}\sum_{m=0}^{k}(1-m)q_n\bar{q}_m e^{i(1-n+m)\theta}\Rightarrow
\end{aligned}\tag{74}$$

$$\begin{aligned}
&\sum_{n=2}^{k}\sum_{m=0}^{k}(1-m)A_n\bar{q}_m e^{i(1-n+m)\theta}+\sum_{m=0}^{k}(1-m)A_0\bar{q}_m e^{i(1+m)\theta}\\
+&\sum_{n=2}^{k}\sum_{m=0}^{k}(1-n)\bar{A}_n q_m e^{i(1-m+n)\theta}+\sum_{m=0}^{k}A_0 q_m e^{i(1-m)\theta}\\
+&\sum_{n=2}^{k}\sum_{m=0}^{k}(1-m)\bar{B}_n\bar{q}_m e^{i(m+n-1)\theta}+\sum_{m=0}^{k}(1-m)B_0\bar{q}_m e^{i(-1+m)\theta}\\
=&\ p_0\sum_{n=0}^{k}\sum_{m=0}^{k}(1-m)q_n\bar{q}_m e^{i(1-n+m)\theta}
\end{aligned}\tag{75}$$

The above can be solved numerically by equating the exponents of equal order. It results in a linear system of 3k-1 equations, or, separating the real from the imaginary parts, 6k-2 equations. The unknowns are 2(k-1) complex coefficients or, equivalently, 4(k-1) real ones. This means that the system is over-constrained, so that the solution to the corresponding least squares problem is evaluated and provides the coefficients of the functions ϕ_1 and χ_1. Alternatively, it would have been possible to evaluate the series to more than k+1 terms. It is selected here to use the same order of approximation for the mapping and for the functions ϕ_1 and χ_1.

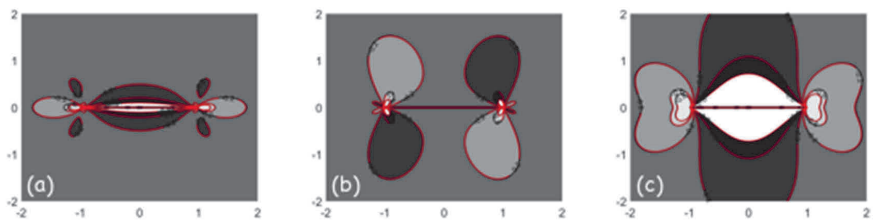

Figure 16. Quasi-analytical approximation results for 26 terms. The filled graph corresponds to the analytical solution for the crack, while the red lines give the corresponding isolines of the numerical solution.

This method does not result in the spurious oscillations observed in the previous case. Increasing number of terms yields increasingly precise approximations of the analytical results. The result in comparison with the analytical solution for a crack with half-length equal to 1 after (Kachanov, 1994) is given in Figure 16. As before the filled areas correspond to the analytical and the isolines to the numerical solution and the stresses depicted are from left to right σ_{xx}, σ_{xy} and σ_{yy}. As may be observed, the agreement is excellent.

4.9 Examples of the stress state estimation

In this section some examples of the results of the algorithm for the stress estimation are presented and the code is validated against analytical solutions and compared to finite element results.

Since the above analytical solution only validates the part linked to the internal pressure, the Kirsch solution for circular openings under biaxial stress and an analytical solution for an elliptical opening under uniaxial far stress field from (Muskhelishvili, 2010) is used to validate the evaluation of the stress distribution resulting from the primary stresses.

For the Kirsch solution a horizontal stress of 1 MPa and a vertical stress of 3 MPa are assumed. A series approximation with 20 terms was used. The results are shown in Figure 17. As may be seen, the absolute error is very small and concentrated around the opening in the form of oscillations. The accuracy is close to the machine precision.

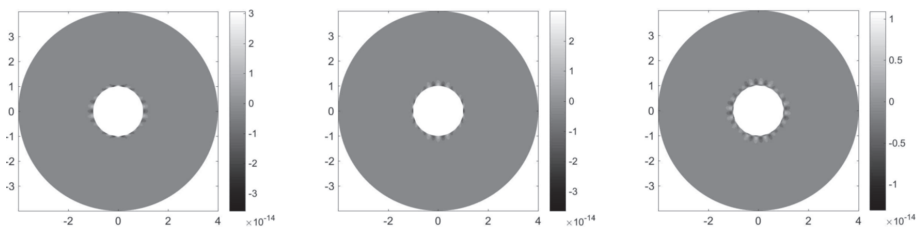

Figure 17. Absolute error of the computed solution with respect to the Kirsch solution. From left to right: σ_{xx}, σ_{xy} and σ_{yy}.

The solution tested next was that of an ellipse with the expression

$$w = R\left(z + \frac{m}{z}\right) \tag{76}$$

with m=0.5. The domain is subjected to far-field horizontal stress with a magnitude of 1 MPa and no vertical stress. 50 terms were used for the approximation. The mapping was evaluated using the algorithm of the previous section and the result was used for the

evaluation of the stress field. The computed solution was compared to the analytical one provided by (Muskhelishvili, 2010) and the absolute error is plotted in Figure 18. As may be observed, the absolute error, which is again concentrated in the vicinity of the opening and shows oscillations, remains at all times smaller than 10^{-7}. The same problem was also tackled using an approximation with 20 terms. In this case the maximum absolute error was of the order of 10^{-2}.

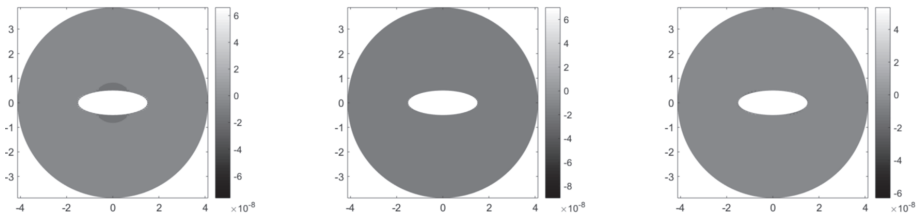

Figure 18. Absolute error of the computed solution with respect to the solution after (Muskhelishvili, 2010).

In Table 2 the maximum error for different shapes of ellipses and for different numbers of terms used for the mapping is shown. m is the parameter present in equation (76), n is the number of discretization points on the boundary and k is the number of terms used for the approximation. Three different times were measured. Time 1 stands for the whole procedure, including the evaluation of the mapping numerically, as well as the evaluation of the analytical solution for comparison. Time 2 stands for the evaluation of the coefficients of the functions ϕ_1 and χ_1. Finally, time 3 stands for the evaluation of the stress state, consisting of the summation of the power series required to evaluate the derivatives of the functions ϕ_1 and χ_1. The first observation to be made is that the maximum error decreases with increasing number of terms as one would expect. It stops decreasing after a certain number of terms, that depends on the shape.

Table 2. Stress state accuracy for different ellipses and different numbers of terms.

m	n	k	Max. error	Time 1 [sec]	Time 2 [sec]	Time 3 [sec]
0.2	1024	25	3.3674e−06	1.974315	0.022092	1.956998
0.2	1024	50	3.3536e−06	3.324643	0.012865	3.302847
0.2	1024	100	3.3536e−06	6.444014	0.026391	6.429781
0.4	1024	25	1.7587e−04	1.744714	0.008909	1.729890
0.4	1024	50	6.5545e−06	3.300635	0.010736	3.286997
0.4	1024	100	6.5587e−06	6.506391	0.022210	6.492972
0.6	1024	25	6.9891e−02	1.717243	0.010161	1.717243

0.6	1024	50	2.8072e−05	3.278999	0.010476	3. 264389
0.6	1024	100	9.0391e−09	6.677930	0.023379	6.663668
0.8	2048	25	2.3687e+00	3.544546	0.009983	3. 519414
0.8	2048	50	9.4072e−01	6.712898	0.012182	6.686189
0.8	2048	100	5.1216e−03	13.97138	0.026864	13.94268

The times were measured at single execution on a personal computer and should thus be considered indicative. Even so, it is clear that the time of execution increases with increasing number of terms and with finer discretizations. Another observation that can be made is that the time required for the evaluation of the series coefficients of the stress functions is only a small fraction of the whole. The largest part of the required time is used for series summation. On the whole, it may be concluded that the method introduced here provides a good approximation of the stress state around openings of an arbitrary shape.

As a next step a comparison of the computed stress state around the borehole by the conformal mapping method and finite element analysis is presented. Three stages of the breakout development are simulated in order to compute the stress redistribution around the borehole. As an exact analytical solution for the mapping does not exist in this case both the mapping algorithm and the algorithm for the stress determination are used. As no analytical solution exists for the stress state, the results of the conformal mapping method are validated against the FEM simulations.

For the FEM simulations the commercial software PLAXIS 2D is utilized. The geometry for the three different simulations (immediately after the drilling of the borehole, when half the depth of the breakout is developed and when the breakout is fully developed) is input-based, so that the elastic solution for the stress state around the borehole and the breakout is directly compared for the two methods based on the same problem geometry.

In the FEM simulations the problem is analyzed as plane strain. However, since in conformal mapping the effect of the out-of-plane stress is not taken into account in this work, a linear elastic constitutive law is used with zero Poisson's ratio (ν=0). The Young's modulus is set to 15 GPa, even though it does not influence the solution for the major and minor principal stress components. A rectangular domain is used with the geometry of the borehole and borehole breakout in the center. Zero displacement boundaries are placed 100 radii away from the borehole, both in the vertical and the horizontal axis, to ensure that the boundary has no effect on the solution (infinite medium). The mesh is refined around the borehole until the solution for the two principal stress components is not influenced by the discretization. 15-noded triangular elements are used in Plaxis 2D.

The results of the simulations as far as the major principal stress component is concerned are presented in Figure 19, for the three stages. The left column (a, c and e) shows the results of the finite elements simulations, while the right column (b, d and f) shows the results of the algorithms discussed above. The results of the conformal mapping method

are in very good agreement with the FEM simulations and give confidence for the applicability of this semi-analytical method both for solution of the direct problem and for the in-situ stress state assessment that is presented in what follows.

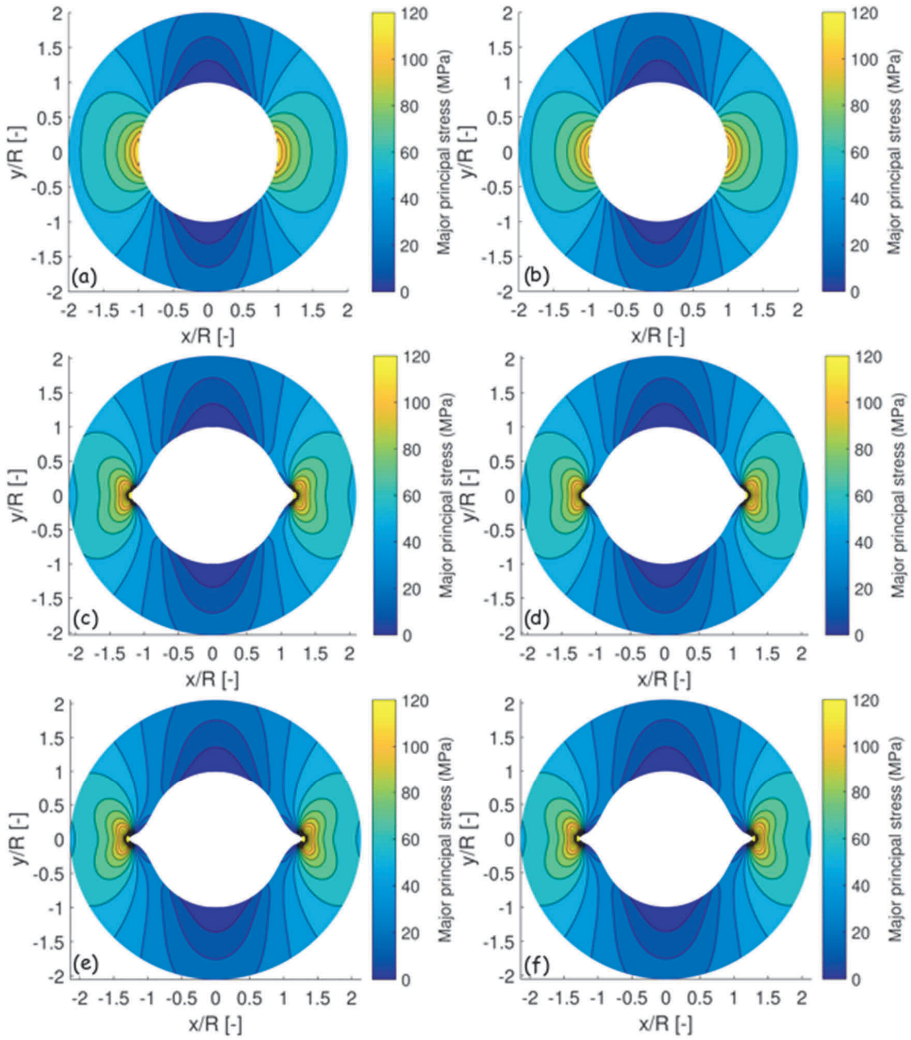

Figure 19. Comparison of FEM and conformal mapping results. The left column (a, c and e) shows the results of the finite elements simulations, while the right column (b, d and f) shows the results of conformal mapping for the same shapes.

5. BREAKOUT GEOMETRY EVALUATION

In this chapter the evaluation of the final geometry of a borehole after the formation of breakouts is presented and discussed. The outline of the code used is given below:

initialize the borehole boundary

discretize the domain

while (new surface > Tol)

evaluate the stress state using conformal mapping

evaluate the yield function

remove the area formed that yielded

discretize the new borehole boundary

end

5.1 Oscillation propagation and smoothing

In this section certain points regarding aspects of the implementation other than the conformal mapping are discussed. A significant point concerns spurious oscillation of the solution in the vicinity of the opening.

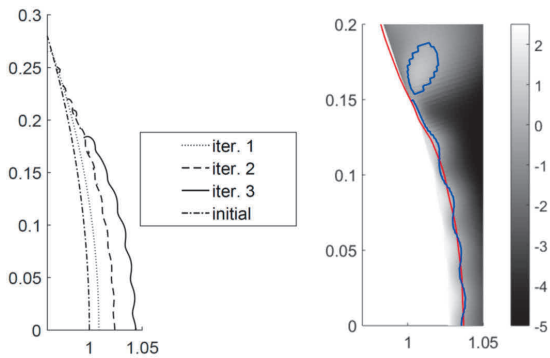

Figure 20. Numerical oscillations. Left: Boundary after successive iterations. Right: Boundary smoothing.

As shown on the left Figure 20, small oscillations that are not visible in the first iteration propagate and increase in amplitude. This is a result of the evolution of the boundary

shape. Small oscillations present in one iteration mean that the boundary of the next iteration exhibits grooves and peaks, which result in stress concentrations that are not present in reality. Such oscillations become more pronounced as the number of terms used for the series expansion expressing the stress functions increases. As decreasing the number of terms of the series expansions however is not practicable beyond a certain point, as it also reduces accuracy, it was selected to use smoothing in the form of a moving average. An example is shown on the right of Figure 20, where the original curve is shown in blue and the smoothed curve is shown in red. It can also be seen that the blue, original, curve shows stepwise variations in its direction. These are a result of the discretization.

Another feature that can be observed is the formation of areas where the criterion for failure is satisfied, but that are located at the interior of the material. It was selected here to ignore such closed curves. They can however just as easily be included.

5.2 Problem position

The outline of the problem considered is presented in Figure 21.

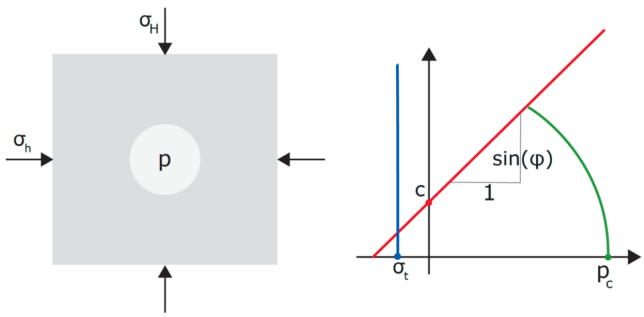

Figure 21. Problem outline. Left: Problem geometry. Right: Failure criterion.

The geometry is shown on the left of Figure 21. The initial borehole radius is set equal to one. This is equivalent to normalizing all length units with the borehole radius. Strictly speaking this is not necessary, as all parts of the method developed here can work with any other size. In the specific case however, there is no loss in generality, as the failure criterion and material response are not scale dependent. The maximum principal stress considered, σ_H, is assumed to act in the vertical direction, while the minimum principal stress, σ_h, is assumed to act in the horizontal one. It should be remarked here that rotating the stress state would simply rotate the results by the same angle and in the same direction. Thus, the orientation of the breakouts is the same as one of the principal directions of the *in situ* stress, in accordance to what has been observed in the field and in the laboratory.

Table 3. Strength parameters.

σ_t [MPa]	c [MPa]	ϕ [°]	p_c [MPa]
6.0	15.0	55	200

The assumed failure criterion is shown on the right of Figure 21. A multi-surface failure criterion (see Figure 21 on the right) was used to render it easy to distinguish between the different modes of failure. A tension cut-off criterion was assumed for tensile failure with a tensile strength of σ_t (in blue on the right of Figure 21), a Mohr-Coulomb criterion for shear failure with a cohesion of c and a friction angle of φ (in red on the right of Figure 21) and a circular segment with a radius of p_c for compaction failure (in green on the right of Figure 21). In all cases arbitrary values were selected for the strength. The values selected for the tensile and shear strength were chosen close to those measured for different types of granite by (Arzúa & Alejano, 2013). The values used are given in Table 3. Each mode of failure is discussed separately in what follows.

5.3 Shear failure

In Figure 22 three examples of results are given.

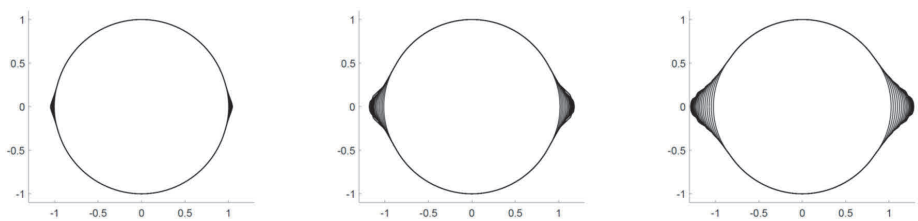

Figure 22. Shear induced breakouts, σ_h=20 MPa. Left: σ_H = 40 MPa. Middle: σ_H = 45 MPa. Right: σ_H = 50 MPa.

The minimum principal stress is set to 20 MPa and maintained constant, while the maximum principal stress ranges from 40 to 50 MPa. The change in both width and depth of the breakouts is easy to note. The different lines in each figure correspond to successive iterations of the code. On the left of Figure 22 they are not visible due to very fine spacing.

A common reason for simulating borehole breakouts is the assessment of the *in situ* stress state. As a rule, based on analytical solutions, only the width can be used, resulting in a linear relationship between the principal stresses, rather than in a value for each of the stresses. Based on the Kirsch solution, the circumferential stress at the wall of the borehole is given by

$$\sigma_{\theta\theta} = (\sigma_H + \sigma_h) + 2(\sigma_H - \sigma_h)\cos(2\theta) \tag{77}$$

Failure takes place when the uniaxial strength is exceeded. Given that, based on observations, the width of the breakout remains constant for constant far field stress while its depth increases, a number of different stress states will result in breakouts with the same width but with different depths. Solving the above for the maximum principal stress yields

$$\sigma_H = \frac{\sigma_{\theta\theta} - (1 - 2\cos(2\theta))\sigma_h}{1 + 2\cos(2\theta)} \tag{78}$$

Substituting the circumferential stress with the uniaxial strength and the angle θ with a selected value yields the locus of stress states resulting in the same width of shear induced breakout. A value of 40° was arbitrarily chosen here and four different stress states were evaluated. They are given in Table 4.

Table 4. Stress states shown in Figure 23.

σ_t [MPa]	c [MPa]	ϕ [°]	p_c [MPa]
6.0	15.0	55	200

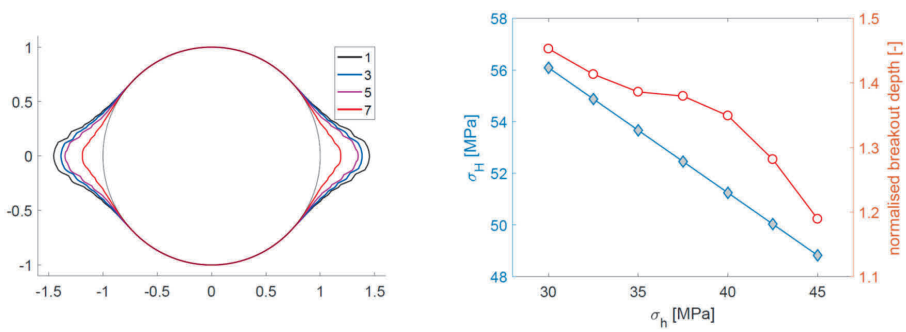

Figure 23. Effect of the stress state on the breakout depth. Left: Breakout shape. Right: Stress state and breakout depth.

The result is shown in Figure 23. On the left of Figure 23 the final shapes of the borehole for four different stress states. The numbers in the legend correspond to the enumerated stress states in Table 5. The initial shape is also provided as reference. As may be seen, the width is the same in all cases, but the depth differs. On the right of Figure 23 the maximum principal stress and the breakout depth are plotted as functions of the minimum principal stress. The corresponding vertical axes are located at the left and the right of the

figure, respectively. It is clear that the variation of the breakout depth is nonlinear but has a one to one correspondence to the maximum principal stress.

Table 5. Stress states illustrated in Figure 23.

number	1	3	5	7
σ_H [MPa]	30	35	40	45
σ_h [MPa]	56.09	53.67	51.24	48.82

On the whole the results for shear failure are satisfactory and encourage the possibility of using a formulation such as the one suggested here for the assessment of the *in situ* stress state on the basis of the shape of borehole breakouts.

5.4 Tensile failure

Two different primary stress states were considered to test the simulation of tension induced failure.

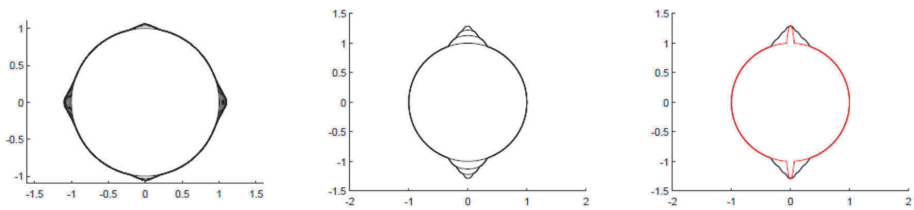

Figure 24. Tension induced breakouts (tensile cracks). Left: $\sigma_H = 40$ MPa, $\sigma_h = 10$ MPa. Middle: $\sigma_H = 20$ MPa, $\sigma_h = 2$ MPa. Right: Alternative geometry.

In the absence of internal pressure, tensile stresses appear only if the stress ratio is larger than 3 or smaller than 1/3. The stress states were selected accordingly to ensure that a tensile breakout occurs. For the first of the two, shown on the left of Figure 24, it can be observed that both shear induced and tension induced failure take place. Simultaneous occurrence and propagation of breakouts at different locations of the borehole wall pose no difficulties for the implementation.

To investigate more easily the tensile failure mode only, the tension cut off criterion was the only one considered for the next simulation. To test the robustness of the implementations a somewhat extreme stress state was selected with a ratio of maximum to minimum principal stress equal to ten. The result is shown in the middle of Figure 24.

While the simulation converges, the breakout shape differs from the slit shaped breakout known from observations.

The borehole with a narrow breakout shown on the right Figure 24 in red and much closer to the typical shape known from observations, was tested under the same stress state. The width was selected small, at 0.1, and the depth was selected equal to the final depth of the breakout shown in the middle of Figure 24. No failure was found to take place for this shape. This indicates that the code either estimates correctly or overestimates the depth of the tensile breakout.

The origin of the discrepancy in shape may be a result of the selection of the failure criterion, but most likely stems from the fact that in the present work the stress disturbance due to the creation of the borehole was assumed to take place instantaneously.

For tensile failure, where the width of the breakout is known to be extremely small, an analytical evaluation of the conformal map would be more suitable. This can be easily calculated using first a projection from the shape of the borehole with a slit-shaped breakout to a slit and subsequently from the slit to the unit circle.

5.5 Compaction failure

Failure due to compaction was investigated next, activating only the part of the yield surface that is linked the compaction induced failure (marked in green on the right of Figure 21).

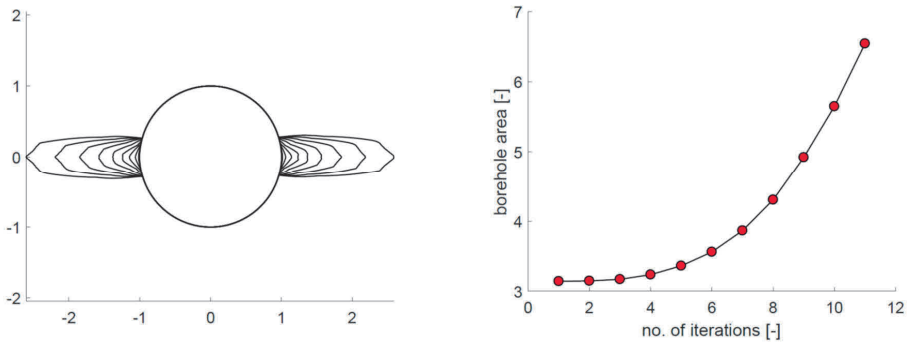

Figure 25. Compaction induced breakouts. Left: Breakout propagation. Right: Borehole surface.

It was found that the width of the breakout remains constant in this case as well, while the depth increases. In contrast to the results of the previous subsections, the area of material failing at each iteration was found to increase and the propagation of the breakout showed no signs of coming to a stop. An example is shown in Figure 25, where the

minimum principal stress was equal to 90 MPa, while the maximum principal stress was equal to 125 MPa.

On the left of Figure 25 the evaluated shape of the borehole after successive iterations is shown. While the shape is consistent with the one known from observation, it is clear that the propagation shows no signs of halting. On the right of Figure 25 the surface of the borehole cross-section (normalized by the square of the borehole radius) is shown as a function of the iterations. The rate of change of the surface seems to be increasing, so that it is obvious that no equilibrium will be reached.

This result may be due to the fact that the material in the present work was considered elastic-perfectly brittle, excluding the possibility of plastic hardening. Another reason for the results observed may be the fact that the out of plane stress was not considered in the calculations in this case. This factor is discussed in what follows.

5.6 Some remarks

As was shown above, different modes of failure can be simulated, even when taking place at the same time. The proposed method can also capture the breakout depth variation for stress states that are characterized by the same breakout width. This suggests that it could provide a valuable tool for the determination of the *in situ* stress state on the basis of the shape of the observed borehole breakouts, making use of both width and depth, in contrast to current practice.

The breakouts resulting from tensile failure simulated here were found to be inconsistent in shape with *in situ* observations. The calculated depth however was shown to be, if not accurate, erring on the safe side. Possible grounds for the discrepancy may be the selection of failure criterion or the instantaneous unloading assumed in the present work. An analytical calculation of the conformal map can provide the slit-shaped breakouts known from observation.

The implementation presented here presents a significant limitation in that it takes into account only the in plane stresses. The out of plane stress is known to affect the shape of borehole breakouts and the fact that it has not been taken into account in the present work may explain the apparently infinite propagation of compaction induced breakouts observed here. The result may however also be due to the fact that no plastic hardening was considered, as the formulation was developed for the elastic- perfectly brittle materials.

On the whole it can be concluded that the methodology presented here provides a promising tool for the simulation of borehole breakouts in brittle materials.

5.7 Effect of the out of plane stress

The effect of the out of plane stress can be incorporated with relative ease into the algorithm, by means of using a failure criterion that takes into account all three principal stresses. For the evaluation of the out of plane stress the plane strain assumption is used. Since the out of plane strain needs to be zero and the changes in the in plane stresses are known, the Poisson's ratio can be used to evaluate the new value of the out of plane stress. Two calibrations are performed, one under the assumption that the out of plane stress has no significant effect on the material response and one under the assumption that the out of plane stress is as important as the in-plane stresses.

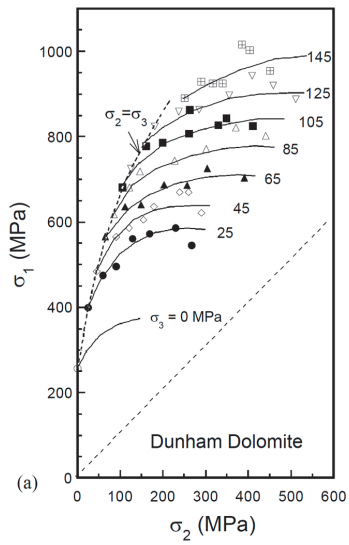

Figure 26. Effect of intermediate stress on the failure envelope (Song, 1998)**.**

In reality the real material response lies somewhere in between, as measured and discussed by Song (Song, 1998). An example of the effect of the intermediate stress on the failure envelope is shown in Figure 26 from polyaxial tests. As can be seen, the strength more than doubles when a triaxial rather than a practically biaxial stress state is considered. The case where the out of plane stress is ignored will be denoted as biaxial stress, while the case where the out of plane stress is considered as important as the in-plane stresses will be denoted as triaxial stress.

For brittle failure ignoring the intermediate stress the Hoek-Brown criterion (Hoek & Brown, 1980) was used. It is expressed in terms of principal stresses and is restricted to two dimensions. It reads

$$\sigma_1 = \sigma_2 + \sigma_u \sqrt{m_i \frac{\sigma_2}{\sigma_u} + 1} \tag{79}$$

where σ_u is the uniaxial compressive strength of the material and m_i is a parameter usually very close to the ratio of the uniaxial compressive strength to the tensile strength.

Two material parameter sets were considered, based on experimental results from triaxial tests on sandstones, of which the first set shows a lower cohesion and a higher friction angle, when compared to the second one. The uniaxial strength was determined experimentally and was found to be equal to 92 MPa for the first case and 99 MPa for the second case. The parameter m_i was determined on the basis of the best fit with experimental results from Brazilian, uniaxial and triaxial tests. The experimental results from Brazilian, uniaxial and triaxial tests, along with the best fit, are shown in Figure 27. The resulting parameters are given in Table 6.

Table 6. Material properties for failure assuming a biaxial stress state.

σ_u [MPa]	m_i [-]	σ_t [MPa]
92	28	3.3
99	8	3.3

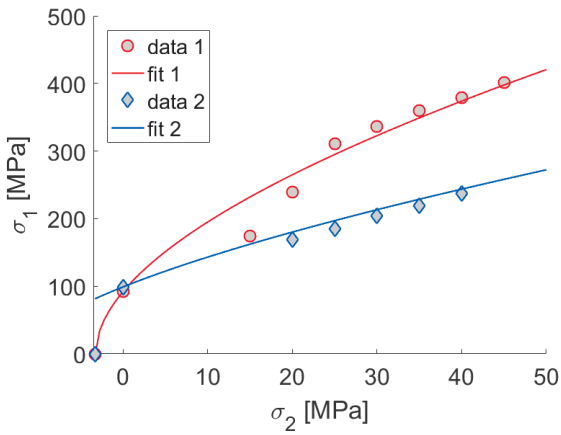

Figure 27. Calibration for the biaxial stress assumption.

For failure accounting for the intermediate stress a different criterion was used (Gerolymatou, 2017). The yield surface has the form

$$f = q^2 + M^2 h(p)(p - p_t)(p - p_c) \tag{80}$$

where

$$p = \frac{1}{3}\mathrm{tr}(\underline{\boldsymbol{\sigma}}) \tag{81}$$

$$q = \sqrt{\frac{3}{2}}\left\|\underline{\boldsymbol{\sigma}} - p\underline{\mathbf{I}}\right\| \tag{82}$$

$$h(p) = \exp\left[-\frac{1}{\beta}\left(\frac{p - p_t}{p_c - p_t} - \alpha\right)^2\right] \tag{83}$$

The constants were evaluated by fitting the experimental results, as seen in Figure 28. The values of each of the constants are given in Table 7. Differences between extension and compression are ignored, as no experimental information is available. Since both criteria are excellent fits of the experimental data, their main difference lies in the consideration of the out of plane stress.

Table 7. Material properties for failure assuming a triaxial stress state.

p_t [MPa]	p_c [MPa]	α [-]	β [-]	M [-]
92	3.3	1.0	0.35	3.0
99	3.3	1.0	0.5	2.0

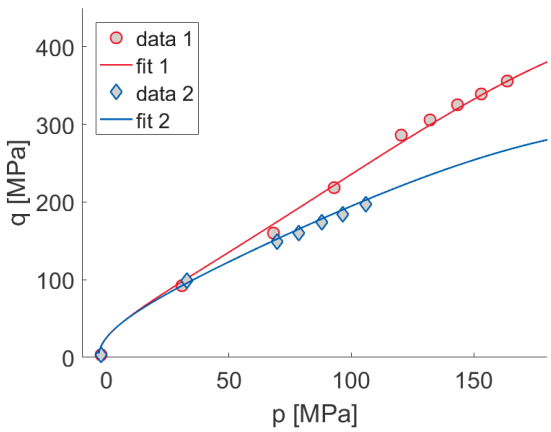

Figure 28. Calibration for the triaxial stress assumption.

5.7.1 First set of material parameters, biaxial stress

Shear failure can take place when the horizontal primary stress is larger than the vertical one, assuming the directions shown in the figures that follow. The vertical stress is maintained equal to 34 MPa and a parametric analysis is performed with respect to the horizontal stress.

The results are shown in Figure 29. On the left the shape of the borehole breakouts for different horizontal stresses is given. As may be observed, both the width and the depth increase with increasing horizontal stress, with the depth increasing however significantly faster than the width. On the right the depth is shown as a function of the horizontal stress. The increase seems to be exponential after an initial quasi linear response, though this is only supported by the last point.

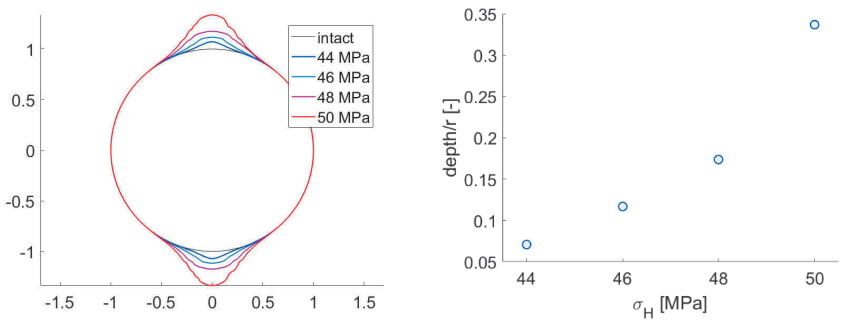

Figure 29. Shape of borehole breakouts (left) and depth of breakouts (right) for different horizontal stresses.

5.7.2 First set of material parameters, triaxial stress

For this set of simulations in addition to the calibrated model parameters, which are given in Table 7, the Poisson's ratio is needed. A value of 0.2 is used here, lying within the

range of reasonable values for an intact rock. The out of plane stress was set equal to the vertical one, namely 34 MPa. The results are shown in Figure 30 below.

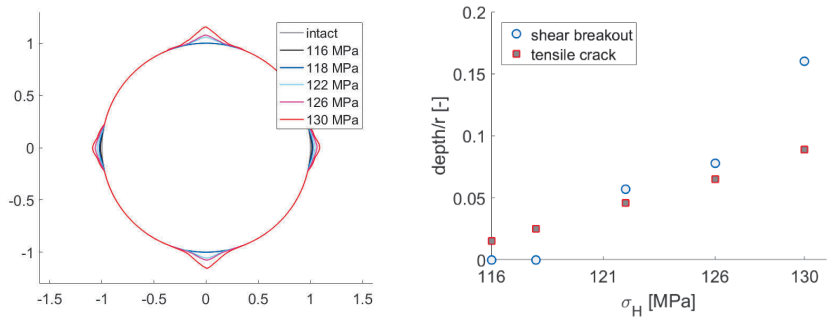

Figure 30. Shape of borehole breakouts (left) and depth of breakouts (right) for different horizontal stresses.

The formation of tensile cracks starts earlier than the formation of shear breakouts. However, with increasing horizontal stress the depth of the shear breakouts increases significantly, while the depth of the tensile cracks does not increase at the same rate. Breakouts are only observed from horizontal stresses equal to 118 MPa, a value that is high and corresponds to a stress ratio of almost 4.

5.7.3 Second set of material parameters, biaxial stress

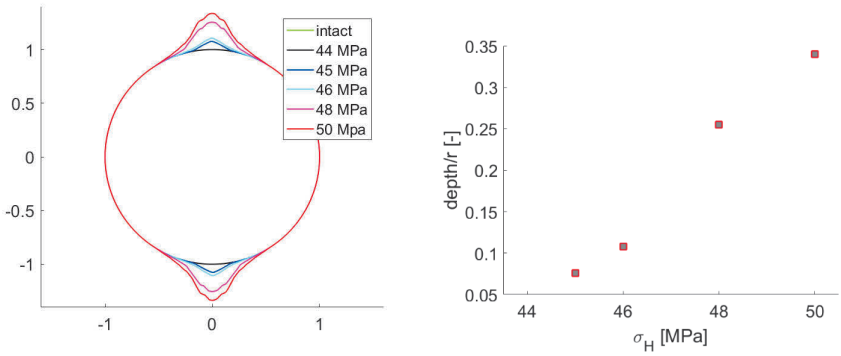

Figure 31. Shape of borehole breakouts (left) and depth of breakouts (right) for different horizontal stresses.

The procedure is repeated for the second set of material. The assumption of biaxial stress is tested first. The results are shown in Figure 31. As far as the shape is concerned, it can

be observed that the results are similar to the ones for the previous material. The formation of the breakouts starts at a higher horizontal stress compared to the first material but increases at a higher rate with increasing horizontal stress. On the right of the same figure the depths of the borehole breakouts are compared for the two materials as a function of the in plane horizontal stress.

5.7.4 Second set of material parameters, triaxial stress

The results for the second material parameter set are evaluated next under the assumption of triaxial stress state. The results are shown in Figure 32. As was the case before, it can be observed that the breakout formation starts at much higher stress levels than before, something that was the case also for the first set of material parameters. It is also interesting to note that in this case, as well as in all previous cases, the breakout depth is a hyper-linear function of the maximum principal stress, independently of which failure criterion is used.

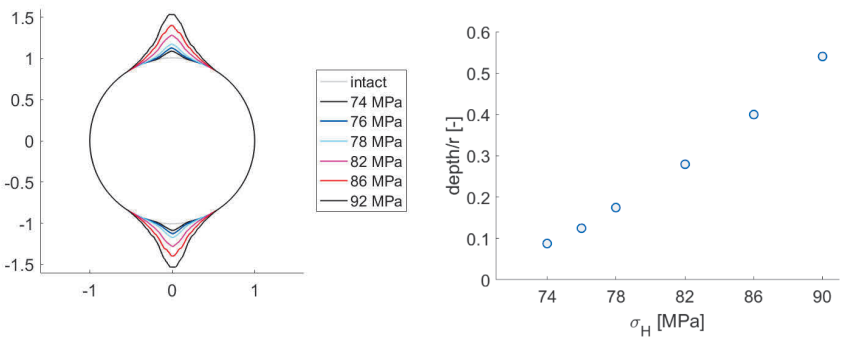

Figure 32. Shape of borehole breakouts (left) and depth of breakouts (right) for different horizontal stresses.

5.7.5 Remarks

From the results of the previous sections it is clear that the consideration of the triaxial stress state results in smaller breakouts. This is also obvious from the very different stress state required to induce the appearance of breakouts, as can be observed from the figure legends. When comparing Figure 29 and Figure 31 to Figure 30 and Figure 32 it is also clear that the first two are similar to each other, while Figure 30 and Figure 32 present several differences. This is due on the one hand to the different stress states used in the simulations, as made clear from the legends of the figures, but also due to the difference

in the material parameters: while the material response is similar for lower stresses, it diverges for higher confining pressures, as illustrated in Figure 28.

On the whole, it seems that the consideration of the out of plane stress results in smaller breakouts by comparing the results presented in Figure 29 to Figure 32. When considering the inverse problem, meaning the evaluation of the *in situ* stress state on the basis of the breakout shape, this means that the commonly made assumption, that only the in plane stresses affect the breakout formation, results in smaller *in situ* stresses than the triaxial stress assumption. This is so because the triaxial stress assumption predicts smaller breakouts than the biaxial stress assumption. This means that, for the same breakout shape, the triaxial stress assumption will result in higher stresses than the biaxial stress assumption. It should also be noted that the biaxial stress assumption underestimates the material strength, thus erring on the side of caution and predicting breakouts that are too large, while the triaxial stress assumption errs in the other direction. The reality lies between the two assumptions, as suggested by the results illustrated in Figure 26.

6. SCALE EFFECTS

In this chapter the scale dependence of the material response is introduced. Some modifications are made in the numerical procedure and the scale effects are introduced after calibration on experimental results.

6.1 Code modifications

To resolve the issue of the spurious oscillations discussed in the previous chapter, which is a numerical one, in the previously used version a smoothing of the boundary was used with an averaging technique. The degree of smoothing was however found to affect the results to some degree. It was chosen here therefore to substitute the smoothing with a polynomial interpolation. An example of the results of the successive iterations is shown on the left of Figure 33. The formed breakout is of the cusp type. The corresponding polynomial interpolation is shown on the right of Figure 33 for a polynomial degree of 5. The interpolation is marked in black, while the original points are marked in red. The agreement between original data and interpolation is good. The results remained the same for polynomial degrees ranging from 3 to 8. A polynomial interpolation of the fifth order is used for subsequent simulations in the present work, unless otherwise stated.

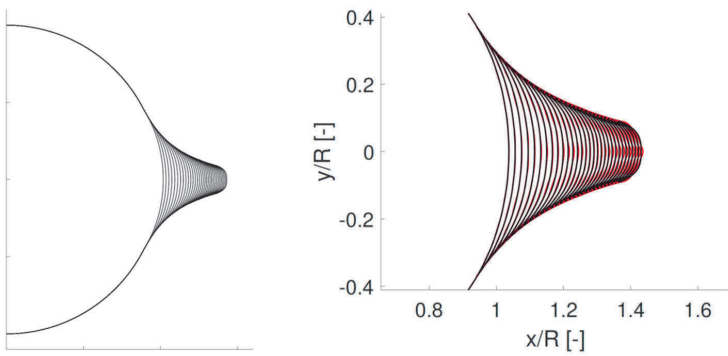

Figure 33. Example of breakout propagation prediction. Left: Breakout propagation. Right: Interpolation.

It was found that using the new approach developed here the breakouts in many cases tend to advance indefinitely as far as the depth is concerned, even if the width remained constant. This phenomenon is known from previous works using methods based on elasticity (Cheatham, 1993; Herrick & Haimson, 1994; P. G. van der Hoek, Smit, & Khodaverdian, 1994). The discrepancy with experimental results is related to the reasons for breakout arrest that were discussed before, namely local plastic response of the host rock, the formation of a process zone or scale effects. It is worth noting that all may be different aspects of the same phenomenon.

For a more thorough explanation of the mechanism leading to continuing breakout propagation, the value of the yield function was plotted as a function of the normalized horizontal coordinate, over a line on the x-axis, for each successive iteration of breakout formation. The result is shown in Figure 34. The arrow indicates the direction of increasing iterations. As may be seen, in the beginning the curve is monotonic, with a gradual decrease. As the breakout propagates, the maximum value of the yield function becomes larger, while its gradient also becomes larger. For later iterations the gradient becomes very pronounced and a local minimum appears. The value of the yield surface changes drastically within a very small area. A plastic rather than brittle response of this area would lead to a very different response and probably arrest the advance.

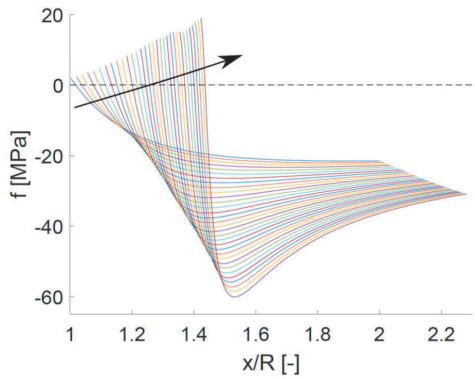

Figure 34. Evolution of the value of the yield function with successive iterations. The values were measured along the line y=0 for positive values of the horizontal coordinate.

6.2 Incorporation of scale effects

As the failure propagates and the breakout becomes deeper, the width of the area that fails becomes smaller. This is akin to the buckling of pillars of ever-decreasing height: the smaller height is linked to size effects, meaning that the load required to reach failure becomes progressively higher. Such scale effects have been observed also in laboratory tests on boreholes, as shown for example in Figure 5.

To incorporate scale effects the results on Alabama limestone by (Herrick & Haimson, 1994) were used. The normalized tangential stress at which failure was first observed is plotted over the hole radius in Figure 35. The stress is normalized with the uniaxial strength of the material. The fit is given by the equation

$$y = max(-1.3 \ln(x/85), 1) \tag{84}$$

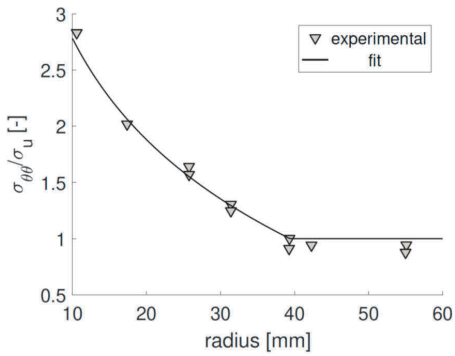

Figure 35. Normalized tangential stress at failure as a function of the borehole radius. Data from Alabama limestone after (Herrick & Haimson, 1994). The fit is given by equation (84).

It should be noted that this is only one of the many options available. It must also be remarked that the cut-off at a value equal to unity is not relevant for the present case, as all experimental points correspond to radii of 11 mm or smaller.

6.3 Comparison to experiments

The semi-analytical method based on conformal mapping is used to simulate experiments performed in the literature on borehole breakout development. The Mohr-Coulomb failure criterion is used to pinpoint the areas that yield during the breakout development. It requires two material properties, i.e. the friction angle ϕ and cohesion c that are calibrated based on experimental results. It reads

$$f = q - \sin(\phi)p - 2c\cos(\phi) \tag{85}$$

where in terms of principal stresses

$$p = \frac{\sigma_1 + \sigma_2}{2} \tag{86}$$

and

$$q = \frac{\sigma_1 - \sigma_2}{2} \tag{87}$$

ϕ is the friction angle and c is the cohesion of the material. The simulated experiments were performed on Alabama limestone and their results are published in (Herrick & Haimson, 1994). For the friction angle a value of 18° was used in accordance to the measurements by (Herrick & Haimson, 1994). The cohesion was calculated as 14 MPa

using the value of the uniaxial compressive strength provided by (Herrick & Haimson, 1994) and the Mohr-Coulomb failure criterion for minimum principal stress equal to zero.

The size effect (as explained in the previous section) is incorporated in the cohesion used in the Mohr-Coulomb failure criterion. For each successive iteration a polynomial fit of the second degree was fitted to the new part of the borehole boundary. The curvature of this polynomial -corresponding on approximation to the curvature of the tip of the breakout- was used to evaluate the equivalent radius. The equivalent radius was subsequently used to evaluate the strength for the next iteration by modifying the cohesion in accordance with the experimental data on Alabama limestone and the fit given in equation (84). An example of the results is shown in Figure 36. As expected, the width remains constant, while the depth increases up to the point of arrest. The failure surfaces of the successive iterations, delimited in the figure with black lines, become gradually smaller. The overall shape is slightly reminiscent of cusp borehole breakouts, though not far from dog-ear shaped ones.

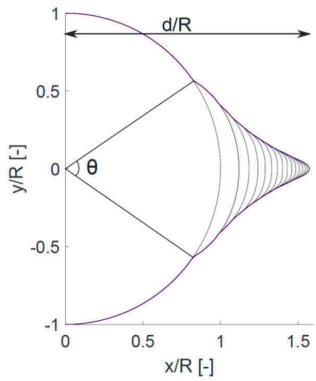

Figure 36. Example of the final shape of the borehole breakout, showing the intermediate shapes for all iterations. As may be observed, the width remains constant, while the depth increases. The overall shape is slightly reminiscent of a cusp.

The first test series by Herrick and Haimson (Herrick & Haimson, 1994) was used for the comparison. Prismatic specimens with a side length of 13 cm in the horizontal and 17 cm in the vertical direction were loaded with the principal stresses in the horizontal and vertical directions. The maximum and the minimum principal stresses were horizontal. A borehole with a radius on 1.1 cm was drilled under load in the vertical direction and the breakout dimensions measured. The aperture angle and the normalized depth were registered, see Figure 36. For the first test series the minimum principal stress was equal to 14 MPa, the vertical stress was equal to 21 MPa and the maximum principal stress varied between 40 and 67 MPa.

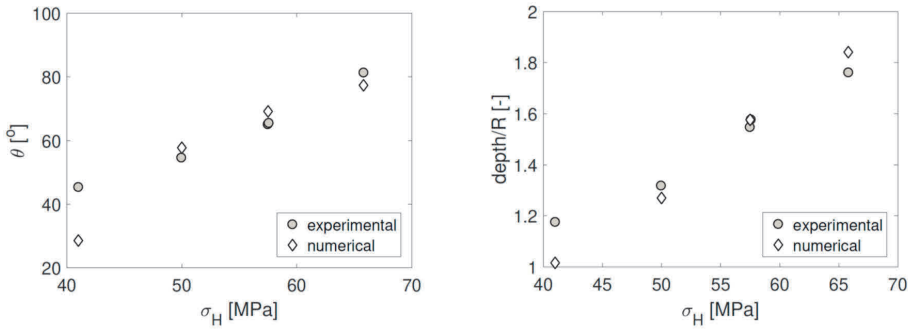

Figure 37. Numerical simulation of borehole breakout development and comparison to experimental results in Alabama limestone. Experimental data after Herrick and Haimson (Herrick & Haimson, 1994). Left: Aperture angle. Right: Normalized depth.

The comparison of the numerical to the experimental results is shown in Figure 37. It should be remarked that, since the breakout width does not increase, the aperture is determined by the Kirsch solution and, of course, the failure criterion. The agreement between numerical and experimental results is rather good, both concerning the aperture angle and the normalized depth, with the exception of the point corresponding to the smallest maximum principal stress. In this case both breakout angle and depth are underestimated. The agreement between experimental and numerical results concerning the depth is particularly good, considering that, since the borehole radius was equal to 1.1 cm, a step of 0.1 in the normalized depth corresponds to a little more than one mm. This agreement indicates that the approach is suitable for the realistic prediction of the shape of borehole breakouts, at least when scale effects are incorporated.

7. *IN SITU* STRESS ASSESSMENT

In this section the inverse problem is considered, namely the evaluation of the stress state based on the geometry of the breakouts, at least when the breakouts are shear induced. The current common practice for the use of borehole breakouts for the assessment of the *in situ* stress state is outlined in Figure 38.

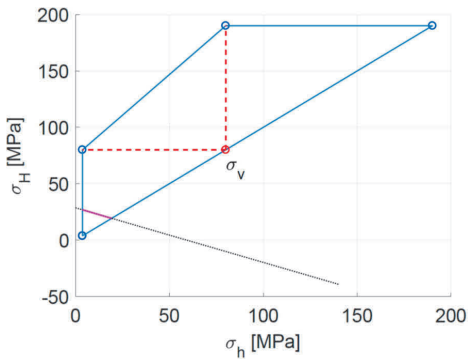

Figure 38. Example of the standard use of borehole breakouts for the estimation of the *in situ* stress state. Based on global failure, the stress state is limited to the interior of the blue polygon. Based on the width of the borehole breakout it is limited to the magenta line.

The Mohr-Coulomb failure criterion with the parameters of Alabama limestone was used, namely a friction angle of 18° and a cohesion of 14 MPa. The vertical stress was assumed to be known and equal to 80 MPa. Commonly in practice the vertical stress is evaluated from the overburden. It is reasoned that the *in situ* stress state cannot be beyond the yield locus of the material. For different assumptions concerning which of the three principal stresses is the maximum and which is the minimum principal stress, different limiting conditions are attained. From them it results that the primary *in situ* stress must be within the polygon marked in blue in Figure 38. From the Kirsch solution for the circular cross-section of the borehole under the assumption of plane strain state, it results that at the wall of the borehole

$$\sigma_H = \frac{\sigma_{\Theta\Theta} - (1 - 2cos(2\Theta))\sigma_h}{1 + 2\cos(2\Theta)} \tag{88}$$

where Θ is the angular coordinate. Setting 2Θ equal to the borehole aperture θ results in

$$\sigma_H = \frac{\sigma_u - (1 - 2cos(\theta))\sigma_h}{1 + 2\cos(\theta)} \tag{89}$$

where σ_u is the uniaxial compressive strength of the material, when ignoring the out of plane stress. The above equation for an aperture of 80° results in the black dotted line of the diagram in Figure 38. Combining with the polygon, it results that the stress state must

lie on the magenta line of the same diagram. A more detailed description may be found in (Zoback et al., 2003). In what follows it will be assessed whether the depth of the breakout can be used in conjunction with its width to further limit the domain of possible stress states, using the conformal mapping methodology presented in the previous chapter for the solution of the direct problem.

7.1 Numerical method for stress assessment

A modified version of the iterative bisection method in conjunction with the conformal mapping algorithm are used to estimate the *in situ* minimum σ_h and maximum σ_H principal horizontal stress components, based on the measured width and depth of the borehole breakout and the strength of the material.

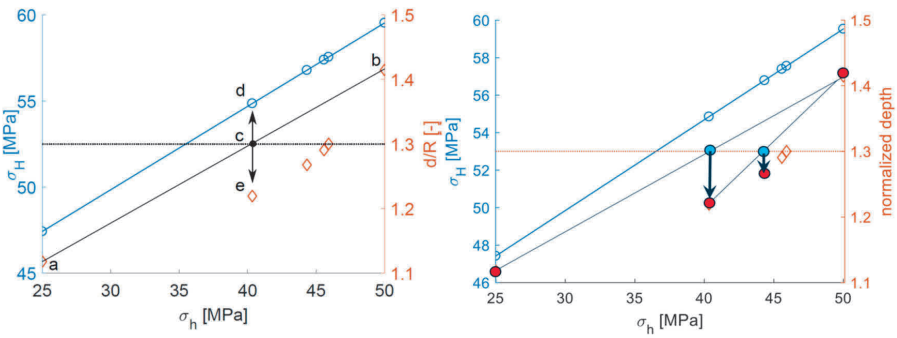

Figure 39. Example of the method for the estimation of the *in situ* stress state. Left: Points a and b are the depths corresponding to the minimum and maximum estimate of the minimum principal stress. The horizontal line is the target depth and point c results from linear interpolation. The corresponding maximum principal stress is at point d and the breakout depth at point e. Points e and b are used for the next steps in lieu of points a and b. Right: Further iterations.

The workflow of the proposed numerical procedure, illustrated in Figure 39, is as follows. An initial guess for the minimum and maximum values of σ_h is provided by the user, denoted also as left and right guess respectively. These two initial guess values can be estimated based on the admissible range as explained for the example of Figure 38 (e.g. the magenta line). Based on the aperture width and the uniaxial strength of the material, σ_H is determined by equation (89) for the two initial guess values of σ_h. Then the conformal mapping algorithm is used to solve the direct problem (see previous chapter) evaluating the depth of the breakouts for the two pairs of σ_h and σ_H. The resulting breakout depths are compared with the target depth value (input borehole breakout depth) and a new interval for the minimum principal stress σ_h is evaluated using the method

described in the next paragraph. The procedure is repeated until a stress state is reached for which the estimated depth is within tolerance of the target breakout depth value. The tolerance is a parameter of the algorithm and is set by the user. In each case presented below, the tolerance used is provided.

In the bisection method, where two initial guess points are also provided, the middle point is used to evaluate the interval in which the solution is to be found for the next iteration, bisecting thus the domain in which the solution is sought. In the proposed numerical procedure, a linear relationship between the minimum *in situ* in plane stress and the breakout depth is assumed in order to evaluate the new guess of the minimum principal stress σ_h for the next iteration, instead of the middle point.

In order to clarify the numerical procedure a graphical example is given in Figure 39. In this example the minimum or left estimate for the minimum *in situ* principal stress equals 25 MPa and the maximum or right estimate for the minimum *in situ* principal stress equals 50 MPa for the first iteration. The corresponding values of the maximum *in situ* stress σ_H are calculated by equation (89) and determine the two blue points with x-coordinates 25 MPa and 50 MPa. The calculated corresponding normalized depth *d/R* is about 1.1, located at point a, (lower than the selected target value of 1.3) and about 1.4, located at point b, (higher than the target value 1.3). Since convergence is not achieved, a third, middle value is selected for the minimum principal stress σ_h by using the intersection of the line between points a and b with the line expressing the target normalized depth, found at point c in the example. For this new value the maximum principal stress σ_H and the normalized breakout depth *d/R* are estimated, corresponding to points d and e respectively. From the three evaluated normalized depths, the new interval for the solution is gained. For the new interval the procedure is repeated until a stress state is reached corresponding to a depth within precision of the target one. The code is outlined in more detail bellow:

provide the following:
  left bracket for the minimum stress shl
  right bracket for the minimum stress shr
  breakout width theta
  breakout depth d

evaluate:
  left bracket maximum stress sHl
  left bracket depth dl
  right bracket maximum stress sHr
  right bracket depth dr

initialize estimated depth dm to zero

while (abs(d-dm) > Tol)

  evaluate the new minimum stress guess shm using

```
    q=(dr-d)/(dr-dl)
    shm=shl+q(shr-shl)
  evaluate the new minimum stress guess sHm
  evaluate the new depth guess dm

  if (d in [dl dm])

    shr=shm
    sHr=sHm
    dr=dm

  else
    shl=shm
    sHl=sHm
    dl=dm

  end

end

return shm, sHm, dm
```

7.2 Results

As an example the case shown in Figure 38 is used. The width of the breakout is set to 80°, while the initial estimates for the minimum and the maximum value of the *in situ* in plane minimum principal stress are 9 MPa and 18.5 MPa respectively. The order of polynomial interpolation for the discretization of the borehole boundary after the removal of the yielded area (see discussion in section 6.1) was set to 3 instead of 5, as this was found to be more stable in the area of low minimum and high maximum principal stresses and close to the area of total failure. The borehole radius was set to 100 mm.

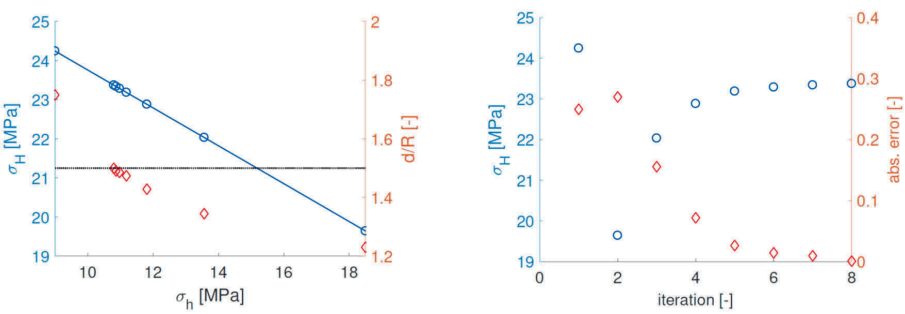

Figure 40. Example of results for target depth 1.5. Left: Results. Right: Convergence.

Two different target depths were tested. The normalized target depth was set equal to 1.5 in the first and 1.6 in the second case. The results are shown in Figure 40 and Figure 41 respectively. On the left of Figure 40 and Figure 41 respectively the estimate of the minimum *in situ* in plane principal stress is shown on the horizontal axis. The left vertical axis corresponds to the estimate of the maximum *in situ* in plane principal stress with the respective data marked in blue, while the right vertical axis corresponds to the normalized depth with the respective data marked in red. On the right of Figure 40 and Figure 41 on the left vertical axis the estimate of the maximum *in situ* in plane principal stress and on the right vertical axis the absolute error of the normalized depth are shown as a function of the number of iterations.

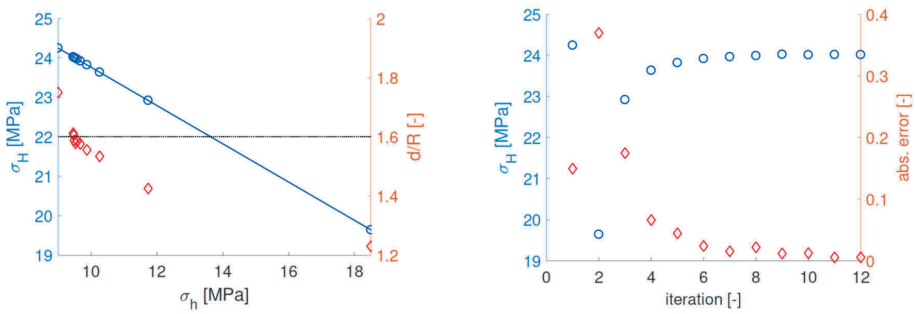

Figure 41. Example of results for target depth 1.6. Left: Results. Right: Convergence.

For the first case 8 iterations were required for a tolerance of 10^{-3}. This includes the initial guesses as iterations. The final values for the minimum and maximum primary stresses were 10.80 MPa and 23.37 MPa respectively, while the corresponding normalized depth was equal to 1.499. It can be seen that the target value is approached monotonically from one side, when ignoring the first iteration. The value of both maximum principal stress and normalized breakout depth changes rapidly in the first iterations and the increments decrease as the number of iterations increases.

The behavior is very similar in the second case. The area corresponding to small minimum principal stresses is however characterized by a very strong variation of the breakout normalized depth and some slight oscillations in the values for the depth may be observed on the left of Figure 41. Despite this, the convergence remains satisfactory, as shown in on the right of the same figure. A number of 12 iterations was required for a tolerance of $5 \cdot 10^{-3}$. The final values for the minimum and maximum primary stresses were 9.48 MPa and 24.01 MPa respectively, while the corresponding normalized depth was equal to 1.605. In this case the normalized depth varies in a much stronger manner than the stresses: a normalized depth of 1.578, evaluated for the eighth iteration, corresponds to a minimum and a maximum primary stress of 9.53 MPa and 23.99 MPa respectively.

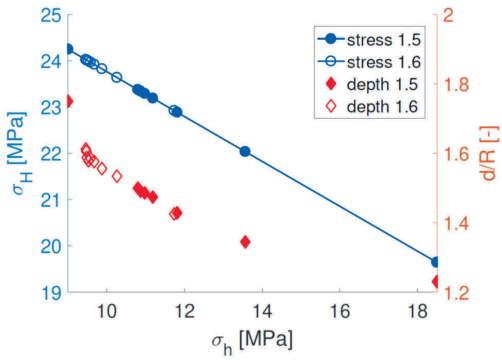

Figure 42. Superposition of the results for the two test cases. Full symbols correspond to a target normalized depth of 1.5, while open symbols correspond to a target normalized depth of 1.6. It can be observed that depth decreases rapidly with increasing minimum principal stress for points close to the left side of the figure.

The results for both cases are plotted together in Figure 42. This highlights the variation of the normalized depth of the breakout with the stresses. For minimum *in situ* in plane principal stresses between 9 MPa and 10 MPa, the normalized breakout depth varies roughly between 1.8 and 1.6, while for minimum principal stresses between 10 MPa and 18 MPa the normalized depth varies roughly between 1.6 and 1.2, showing a much slower variation.

The breakout shape, including the successive iterations to evaluate it, is shown in Figure 43 for the initial guesses, which are the same for the two cases. It can be seen that while the width is the same, the depth is very different. However, at the same time it should be observed that for the borehole shape marked in blue the depth close to the area of the borehole wall that remains sound is very small. Another interesting observation, particularly obvious in the larger breakout, is that the breakouts are dog-ear shaped. For the small scale simulations the breakouts are instead cusp shaped, as shown in Figure 36. This is very likely a scale effect, as the same phenomenon has been observed in the laboratory, with smaller boreholes forming cusp-shaped breakouts and larger ones forming dog-ear-shaped ones.

On the whole the performance of the procedure for the evaluation of the primary stress state using the shape of the borehole breakouts may be deemed satisfactory. In the next section the feasibility of the stress assessment is discussed on the basis of experimental results.

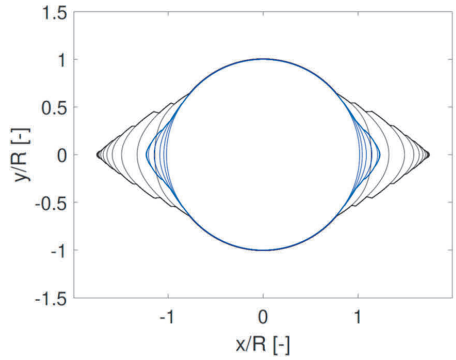

Figure 43. Breakout shape for the initial guesses. It can be seen that while the width is the same, the depth is very different. Moreover, in contrast to the small-scale simulation, the breakouts are dog-ear shaped instead of cusp shaped.

7.3 Discussion on the feasibility of stress assessment

Though the opinion voiced in (Gough & Bell, 1982) that the shape of the borehole breakouts depends solely on the material properties and not on the *in situ* stress state has been shown through experimental results not to reflect reality, it is as yet unclear whether the depth and the width of borehole breakouts are independent from each other. It has been postulated (Herrick & Haimson, 1994; Song, 1998) that, while they both depend on the stress state, they vary in the same manner with it. This would mean that each time either the depth or the width of the borehole breakout may be used for the stress assessment, as the use of the one renders the use of the other automatically redundant. This in turn means that one relationship for the stresses may be gained from the shape of the breakouts, rather than two, as done in the previous section, even using both the breakout depth and the breakout width.

Herrick and Haimson (Herrick & Haimson, 1994) and Song (Song, 1998) reached this conclusion on the basis of results of tests performed in the laboratory. These results are presented in Figure 44. The experimental program by (Herrick & Haimson, 1994) was previously discussed in some detail. On the left of Figure 44 the normalized depth is plotted as a function of the aperture angle for all tested stress states. It can be observed that the width of the distribution of the points, which is close to linear, is rather narrow. This in turn implies that knowledge of the width is equivalent to knowledge of the depth and no additional information may be gained by the use of both.

Song (Song, 1998) performed a large number of tests on Westerly granite, that are plotted on the right of Figure 44. The maximum principal stress was acting in the horizontal direction, with the borehole cored in the vertical direction. Its values lay between 140 and 240 MPa. The minimum principal horizontal stress and the vertical stress were significantly smaller and ranged between 20 and 50 MPa and 20 and 120 MPa

respectively. Once more, the results lie on a relatively narrow band, which is similar to the one observed on the left of Figure 44, especially when taking into account the difference of the limits of the axes for the two graphs. It should be remarked that the results by (Song, 1998) correspond to significantly smaller aperture angles and depths and that the minimum horizontal principal stress was in all cases significantly smaller than the maximum one.

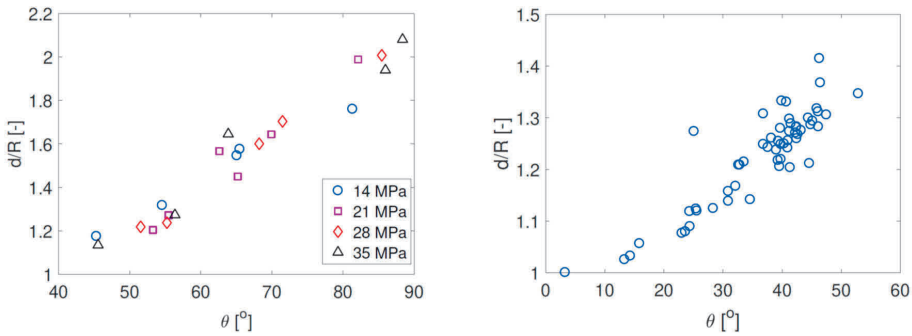

Figure 44. Borehole breakout normalized depth as a function of the breakout width. Left: Results on Alabama limestone by (Herrick & Haimson, 1994). Right: Results on Westerly granite by (Song, 1998).

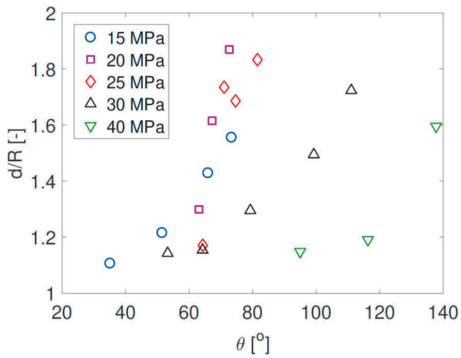

Figure 45. Borehole breakout normalized depth as a function of the breakout width for different far field stress states by (Haimson & Lee, 2004). The vertical stress for the different sets marked in the legend was equal to 30, 40, 40, 40, 50 MPa from top to bottom.

In contrast to the findings discussed above, the results by Haimson and Lee (Haimson & Lee, 2004) on Tablerock sandstone do show a one to one relationship between breakout aperture width and normalized depth, as may be seen in Figure 45. Even in this case it should however be remarked that the results of the three first test series are located in a rather narrow domain. The differences observed indicate that in some cases at least different information is included in the two quantities describing breakout shape. It remains unclear however, why this variation was not present in the previous cases. In the case of (Song, 1998) it may attributed to the small variation of the minimum principal stress, when compared to the maximum principal stress, though this is only an assumption.

The numerical results, as shown for example in Figure 40 or Figure 41, show a significant variation of the normalized depth with constant breakout width. The discrepancy may be due to the selection of the stress states tested in the laboratory or to the fact that a failure criterion not incorporating the out of plane stress was used.

8. BRIE DATA AND COMPARISON

The Bentonite Rock Interaction Experiment, BRIE, was set in the Äspo Hard Rock Laboratory and focused on the hydraulic interaction between the system components of compacted bentonite and the near-field host rock composed of hard and fractured bedrock. The experiment aimed at investigating the exchange of water across the bentonite-rock interface and was conceived in the framework of the research efforts for a future deep underground repository for high-grade nuclear waste. The multibarrier Swedish concept for nuclear waste underground storage includes a natural barrier, the crystalline bedrock, and two engineered barriers, a bentonite buffer and a copper canister.

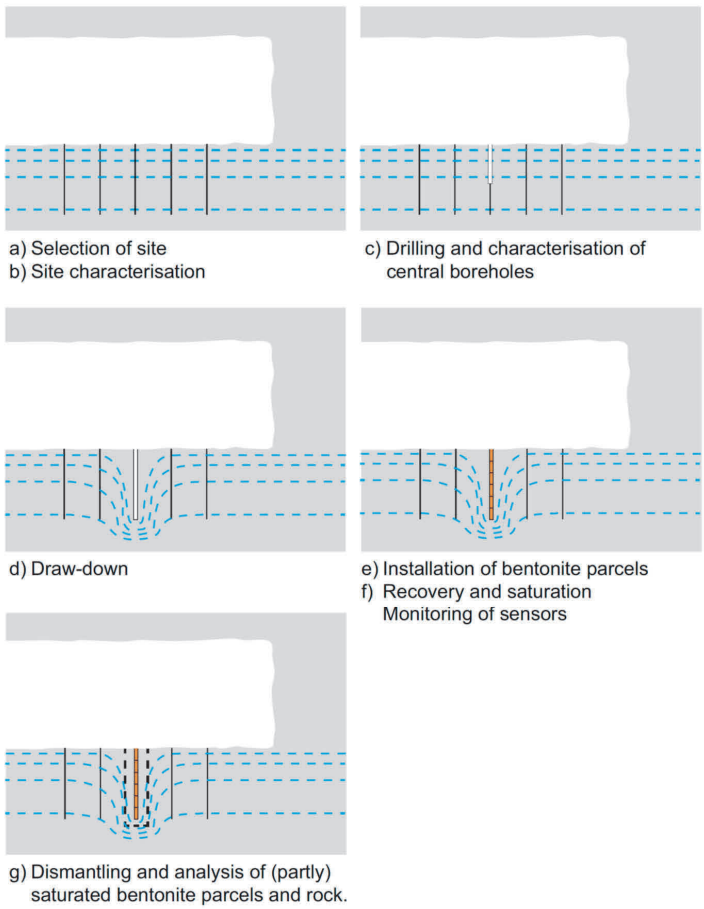

Figure 46. Outline of the BRIE project after (Fransson et al., 2017).

The outline of the project is shown in Figure 46. Within the frame of BRIE, two boreholes were cored (diamond-drilled) and the cores were investigated for fractures. Subsequently bentonite parcels were installed in the boreholes. The hydration of the bentonite parcels was monitored. When the test was concluded, the boreholes were overcored and the bentonite parcels were dismantled. The overcored samples were again investigated (in further detail) for fractures.

This chapter aims to assess the applicability of the approach suggested in this report to real project data. The purpose is not to provide a full validation but to demonstrate how the approach can be used as an indication and guidance for increased understanding linking geological mapping, hydrogeological observations and possible (likely) rock stresses. An extensive description may be found in the project report (Fransson, Åkesson, & Andersson, 2017), while a more abbreviated description is given in (Fransson, Lönnqvist, & Viola, 2019). The sections below describe the stepwise procedure in further detail.

8.1 Geological setting

The Äspö Hard Rock Laboratory (HRL) is located in southeast Sweden, in the Misterhult Archipelago and close to the Oskarshamn nuclear power plant. Its scope is the development and testing of different technologies and methods for studying rock, designing the repository for nuclear waste and depositing the canisters. The BRIE site is located in the TASO tunnel, see Figure 47, at approximately 420 m depth. The boreholes investigated, see detail of area (A) in Figure 48, have shown gabbroid-dioritoid and fine-grained granite as main rock types. In addition, rock occurrences (veins and dykes) with pegmatite and fine-grained granite were identified.

Stress measurements from previous works (Janson & Stigsson, 2002; Thörn, 2013) conclude that the ranges for the *in situ* stresses are:

- σ_H: 16–26 MPa (trend 140–155°)
- σ_h: 9–14 MPa
- σ_v: 10.5–18.1 MPa.

The rock is characterized by a Young's modulus of 76 MPa, a Poisson's ratio of 0.25 and a tensile strength of 14.3 MPa.

Other sources, such as (Hakala, Siren, Kemppainen, Christiansson, & Martin, 2013), give a wider range for the principal stresses, namely

- σ_H: 24+/–5 MPa
- σ_h: 10–18 MPa
- σ_v: 10–20 MPa.

In this case the Young's modulus is reported as ranging from 50 to 80 GPa and depending on the orientation, with lower values in the vertical direction. The Poisson's ratio was found to range from 0.2 to 0.3 and to show little dependence on the direction.

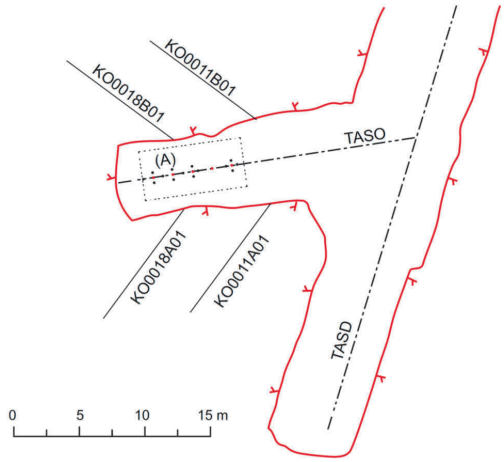

Figure 47. Site outline after (Fransson et al., 2017).

The outline of the site after (Fransson et al., 2017) is shown in Figure 47, with the marked area A shown magnified in Figure 48.

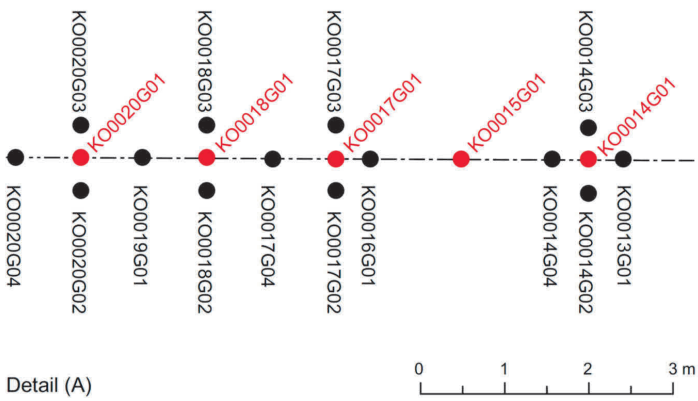

Figure 48. Borehole placement after (Fransson et al., 2017).

The boreholes marked in red were drilled first with a diameter of 76 mm, for selection of site and for site characterization, see Figure 46a and b. The boreholes marked in black followed, also with an initial diameter of 76 mm. Subsequently boreholes KO0017G01 and KO0018G01 were extended to a diameter of 300 mm with a depth of about 3 m, see drilling and characterization of central boreholes, Figure 46c. The distance between the boreholes marked in red was equal to 1.5 m, while the distance between black and red boreholes was either 0.4 m or 0.75 m. This was followed by installation of bentonite parcels; recovery and saturation including monitoring of sensors (Figure 46e and f) and finally; dismantling and analysis of (partly) saturated bentonite parcels and rock, Figure 46g and Figure 50.

The initial boreholes (cores from 300 mm boreholes) showed no continuous fractures as indicated by e.g. the wet trace at the angle 288º (internal orientation) in Figure 49, though other, pre-existing, fractures were observed. After dismantling however, a number of vertical, not previously identified, fractures with pronounced wetting were seen on and inside the bentonite (see lower part of bentonite with internal orientation 0°, 288° and 216°, Figure 49). Based on a compilation of detailed mapping of the cores from the 300 mm boreholes (detailed mapping performed using dye), the main part of the wetted and vertical traces that were interpreted from bentonite, see Figure 49, were not identified on the core. These fractures are more or less perpendicular or parallel to the tunnel and also close to in line with adjacent boreholes (secondary boreholes, see Figure 48 and Figure 50). One possibility could be tensile fractures due to the minimum circumferential stress becoming negative. These fractures would occur as pairs of mutually opposed, vertically dipping conductive fractures.

Figure 49. After (Fransson et al., 2017), lower part of bentonite parcels from KO0018G01 with wetting marks after their extraction. Bentonite blocks 1 to 12 identified on the right hand side of the illustration,

The method used for the dismantling was stitch drilling to cut the periphery and wire sawing to cut the bottom. The final result is shown in Figure 50.

Figure 50. Boreholes after dismantling. KO0017G01 on the left and KO0018G01 on the right. The additional fractures are marked in white arrows.

The type of bentonite used was MX-80 with a requirement of dry density of 1562 kg/m^3. At this dry density and with distilled water the maximum swelling pressure of bentonite is about 10 MPa (Karnland, Olsson, & Nilsson, 2006). According to the same work, at this dry density the swelling pressure is not sensitive to the presence of anions and cations and even high concentrations do not reduce the swelling pressure significantly. It should be noted that these pressures correspond to saturated materials. In the specific case the degree of saturation ranged from 0.5 to 1.0.

8.2 Modelling stages

The stress state is initially evaluated after the excavation of the 300 mm boreholes, see Figure 46c. It is assumed that no failure has taken place before this point, as no (continuous) and possibly coring induced fractures were observed on the cores after the expansion of the two test boreholes to 300 mm diameter. The assumption is that the coring or the coring and swelling (see below) would result in induced fractures. The theory of elasticity is used for the evaluation of the stress state.

Subsequently the installation of the bentonite parcels is considered, Figure 46e. It is investigated whether the swelling pressure from the bentonite parcels may have induced the observed fractures.

In a final stage the effect of the overcoring is considered and it is investigated whether the fractures may have originated in that stage, Figure 46g and Figure 50.

After that the tool based on conformal mapping is used to assess which stress states lead to results compatible with the observations made *in situ* within the frame of the BRIE project.

8.3 Model

8.3.1 Stage 1

The orientation of the tunnel TASO with respect to the North is shown in Figure 51. The trend of the maximum principal horizontal stress lies between 140 and 155°, as already mentioned above. This results in a deviation of the trend of the maximum principal horizontal stress from the tunnel axis that lies between 68° and 83°, as shown in Figure 52.

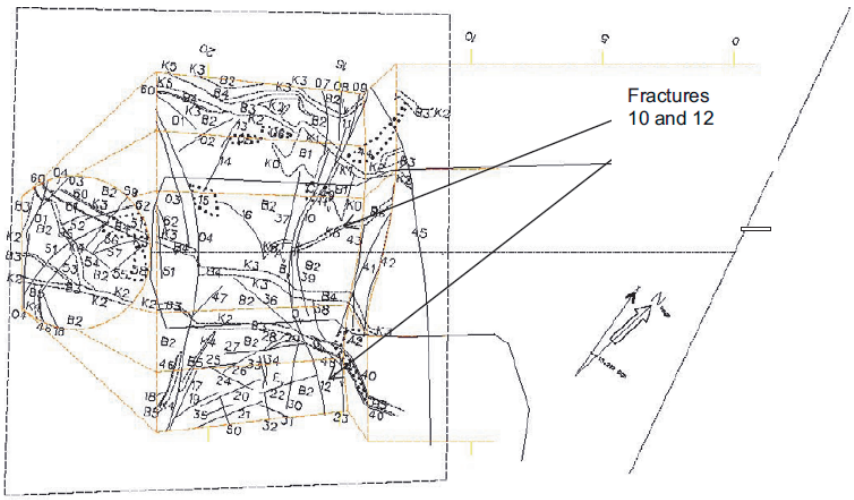

Figure 51. Orientation of the tunnel with respect to the North.

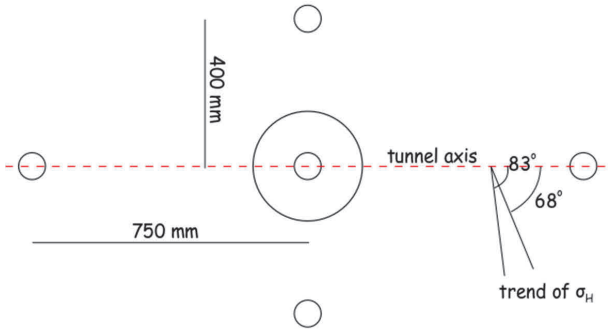

Figure 52. Model geometry including trend of the maximum principal horizontal stress.

The tunnel has a diameter of 5 m and its creation led to a disturbance of the initial stress field. To evaluate the secondary stress state, the stress is decomposed into in-plane and out of plane components. The vertical stress will be the vertical in-plane component, while the horizontal in-plane component will be equal to

$$\sigma_{hi0} = \frac{\sigma_H + \sigma_h}{2} + \frac{\sigma_H - \sigma_h}{2} \cos(2(90^o - \theta)) \tag{90}$$

using the usual transformation law from the circle of Mohr and where σ_{hi0} stands for the horizontal in-plane stress in the undisturbed state and θ is the angle between stress trend and tunnel axis (between 68° and 83°). In the same way the out-of-plane components will be

$$\sigma_{ho0} = \frac{\sigma_H + \sigma_h}{2} + \frac{\sigma_H - \sigma_h}{2} \cos(2\theta) \tag{91}$$

$$\tau_{ho0} = \frac{\sigma_H - \sigma_h}{2} \sin(2\theta) \tag{92}$$

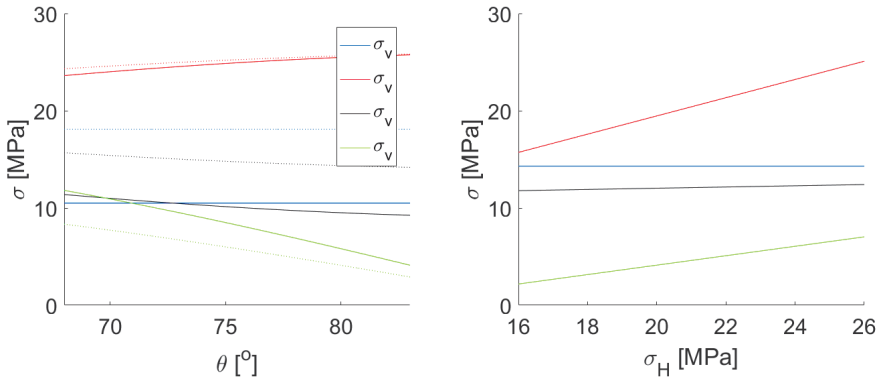

Figure 53. Parametric analysis of the values of the undisturbed stress state.

The values of these stresses under different considerations are shown in Figure 53. On the left the values of the principal stresses are assumed to be known and the angle is varied. For the continuous lines of the left subfigure the set (σv=10.5 MPa, σH=26 MPa, σh=9 MPa) was used, while for the dotted lines the set (σv=18.1 MPa, σH=26 MPa, σh=14 MPa) was used. In the right subfigure the average values from the literature were used for all quantities, except for the principal horizontal stress. It can be observed in the figure that in this case the variation is more pronounced.

In the disturbed stress state, the stresses along the vertical direction are principally of interest, as the considered boreholes cored for the BRIE project were vertical. The redistributed stress field then can be evaluated as

$$\sigma_{rr} = \frac{1}{2}\left[(\sigma_{hi0} + \sigma_v)\left(1 - a^2\right) + (\sigma_{hi0} - \sigma_v)\left(1 - 4a^2 + 3a^4\right)\right] \tag{93}$$

$$\sigma_{\theta\theta} = \frac{1}{2}\left[(\sigma_{hi0} + \sigma_v)\left(1 + a^2\right) + (\sigma_{hi0} - \sigma_v)\left(1 + 3a^4\right)\right] \tag{94}$$

$$\sigma_{r\theta} = 0 \tag{95}$$

$$\sigma_{op} = \sigma_{ho0} + 2\nu\,(\sigma_{hi0} - \sigma_v)\left(-a^2\right) \tag{96}$$

$$\tau_{rh} = 0 \tag{97}$$

$$\tau_{\theta h} = -\tau_{ho0}\left(1 + a^2\right) \tag{98}$$

where

$$a = \frac{R}{r} \tag{99}$$

For the new boreholes the out-of-plane stress is σ_{rr} from equation (93) and the in-plane-stress results from the combination of $\sigma_{\theta\theta}$, σ_{op} and $\tau_{\theta h}$ from equations (94) to (98). Since the tunnel radius is 5 m and the length of the new boreholes is 300 cm, the value of a will vary between 0 and 0.6. Examples of results for the maximum and minimum in-plane stresses for the new boreholes are given in Figure 54.

In all cases an angle of 83° was used. This angle seems more likely based on the orientations of the fractures observed *in situ*. The different initial stresses used were:

- Continuous line: (σv=10.5 MPa, σH=26 MPa, σh=9 MPa)
- Dotted line: (σv=10.5 MPa, σH=26 MPa, σh=14 MPa)
- Dashed line: (σv=18.1 MPa, σH=26 MPa, σh=14 MPa)
- Dash-dotted line: (σv=18.1 MPa, σH=16 MPa, σh=9 MPa)

It can be observed that in all cases the maximum stress is above and the minimum below 15 MPa, though this may be a result of the choices made here. It should also be noted that the angle of deviation of the principal stress directions varies with the initial stress state and ranges in this case between 15° and 30°. For an angle of 68° the angle of deviation for the same cases varies between 27° and 45°.

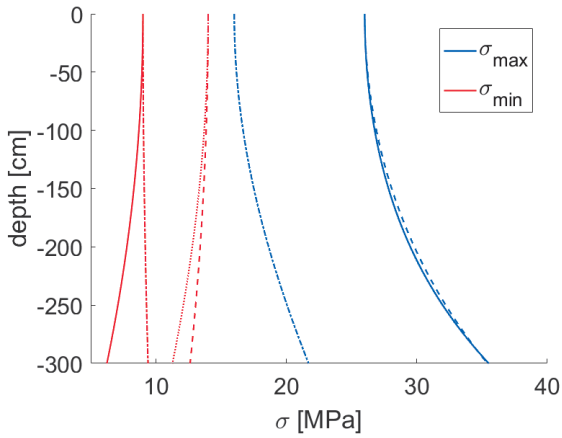

Figure 54. Maximum and minimum in-plane stress estimates for the vertical boreholes. Depth indicates depth below the floor of the tunnel.

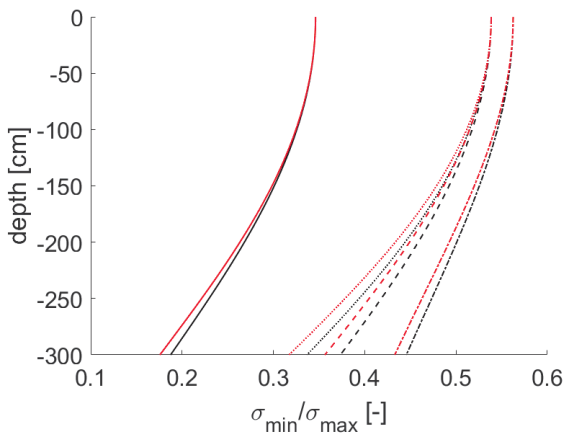

Figure 55. Estimated stress ratios. Black, angle of 83°. Red, angle of 68°. Depth indicates depth below the floor of the tunnel.

The stress ratios for the same cases are shown in Figure 55. In black the stress ratios for an angle of 83° and in red for an angle of 68° are shown. It is known that tensile stresses occur for stress ratios lower than 1/3, which seems to be often the case here. It is also interesting to note, that for most curves the stress ratio at the bottom of the borehole seems to be lower than the stress ratio at the top.

From this analysis it is concluded that the stress state is such that it could lead to tensile failure of the borehole wall, or at least to the presence of tensile stresses at the borehole wall. For the cases examined before the minimum circumferential stress at the borehole wall is shown as a function of depth in Figure 56. For both angles only the first stress scenario leads to cracks. The differences in terms of magnitude are small. However, for the angle of 83°, the orientation of the fractures is in agreement with the one observed in the site. In such a scenario it is likely that the tensile fractures formed later under the effect of the swelling pressure of the bentonite parcels. It should however be remarked that a time delayed formation of the tensile fractures also without the influence of the swelling from the bentonite, cannot be excluded, as it is known that it can take time for the stresses in rock to redistribute and failure to become apparent (Amitrano & Helmstetter, 2006; Savage & Mohanty, 1969; Wawersik & Brown, 1973).

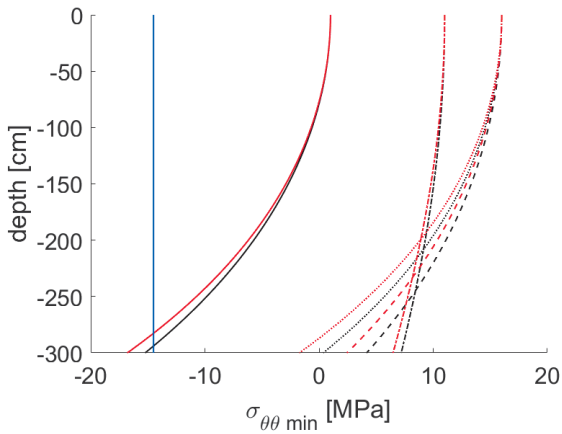

Figure 56. Minimum circumferential stress. Red, angle of 83°. Black, angle of 68°. The blue line marks the tensile strength of the rock. Depth indicates depth below the floor of the tunnel.

Observations from BRIE indicate a stress ratio at the bottom of the borehole being lower than the stress ratio at the top. Based on contour plots of water content, "inward directed" gradients were identified in bentonite block number 5 in the lower part of KO0018G01 (see block 1 to 12 in Figure 49), indicating inflow from the rock wall. The highest water content coincides with one of the dark, wetted trace in the photograph and it was suggested that this may be caused by fracture flow from non-registered fractures (rather than rock matrix flow).

For borehole KO0017G01, the water content in the lower blocks were affected and was most pronounced in (internal) directions 72 and 288°. This coincided with the pegmatite

vein close to these directions (the vein as well being close to perpendicular to the tunnel). At a smaller depth (above the water-bearing vein) in borehole KO0017G01, a very slow increase in RH appeared to be caused by moisture transfer from one of the major fractures in the section below (indicated by the major gradient in water content). The section at a smaller depth, with a slow increase in RH is also a section with a low water content and seemingly no obvious water-bearing feature along the fracture wall (as seen in KO0018G01).

It is examined next whether the small boreholes could disturb the stress state to the extent of influencing the orientation of the tensile fractures. The model geometry assumed in the tunnel is the one shown in Figure 52. The question needing to be answered is whether the boreholes surrounding the principal one could have a significant effect on the stress state acting on the principal borehole. The nearest borehole to the central one is located at a distance of 400 mm center to center. Since the radius of the central borehole is 150 mm, this corresponds to r = 250 mm. The radius of the borehole is 38 mm. Considering this and different stress scenarios, it results that disturbances are at most of the order of 1 to 2 MPa and should therefore only have a slight effect on the stress state and its orientation.

8.3.2 Stage 2

From the result of the previous section it is clear that the effect of the swelling pressure from the bentonite may have induced the tensile fractures observed after dismantling. Considering again the cases of the previous section, the minimum circumferential stresses now become those shown in the previous section further reduced by 10 MPa, under the assumption that the bentonite is saturated. The value of the swelling pressure naturally becomes smaller for lower degrees of saturation but should still be higher than 5 MPa at a degree of saturation of 0.5. The results for the circumferential stresses along with the tensile strength are shown in Figure 57 under the assumption that the value of the swelling pressure was equal to 10 MPa.

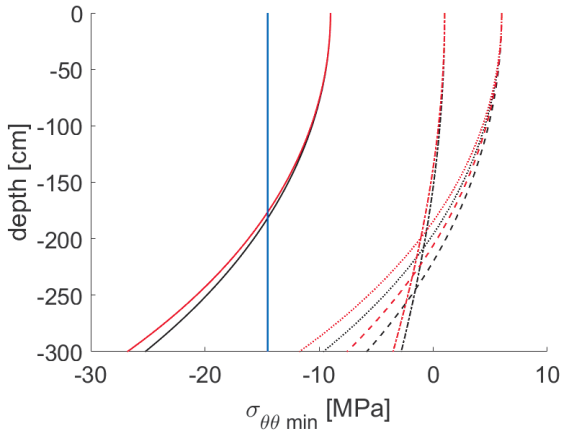

Figure 57. Minimum circumferential stress. Red, angle of 83°. Black, angle of 68°. The blue line marks the tensile strength of the rock. Depth indicates depth below the floor of the tunnel.

8.3.3 Stage 3

Given the amount of uncertainty present in the stress state and the uncertainty concerning the order in which the stitch sawing was performed, it is hard to assess the effect of the dismantling on the formation of the cracks observed. It is however clear that the process along with the accompanying vibrations may have caused some relative displacement in the cracks. It is very unlikely that they were all created at this stage, since some of the wetting marks on the bentonite parcels indicate that they have been present for some time.

8.4 Assessment of likely stress states

8.4.1 Stress field orientation

A first significant point concerns the orientation of the stress field. The analysis presented above indicates that the reason for the creation of the tensile cracks is most likely the presence of tensile stresses. As such fractures are aligned to the local principal stress directions, it is concluded here that the trend of the maximum principal in situ stress is most likely to be 155°.

8.4.2 Stress magnitudes

Given that the stress orientation selected means that the stress state is practically coaxial to the tunnel, the two components principally governing the maximum in-plane stress for

the 300 mm boreholes are the vertical stress and the maximum horizontal stress. The minimum in-plane stress for the 300 mm boreholes is governed primarily by the minimum horizontal stress. High tensile stresses are expected to arise and to be large in magnitude in the areas of interest when the stress anisotropy is large between the vertical and the maximum horizontal stresses when both are characterized by high values and when the minimum horizontal stress is small. This in turn means that both strike-slip and reverse type stress states are possible.

The magnitude of the stress can be delimited using the tool developed within the frame of the present project. In terms of information from the site two main types are required: the location in the borehole at which the cracks were observed and, ideally, the depth of the cracks. In the present case, it is known that the cracks were observed towards the deeper part of the borehole. The depth of the fractures is not known. For the sake of illustration, it is assumed that the cracks were observed from a depth of 250 cm to the bottom of the borehole and that their depth is known. To simplify the process and given that the likely trend only weakly affects the stresses, as shown in Figure 56 and Figure 57, it is assumed that the trend of the maximum horizontal stress is perpendicular to the tunnel axis. Using the analytical considerations presented above, these assumptions result in the equation

$$\sigma_t = 3.00\sigma_h - 1.59\sigma_H + 0.34\sigma_v - p \tag{100}$$

where σ_t is the tensile strength of the rock, which is known and equal to -14.3 MPa, and p is the bentonite pressure, which may or may not be used depending on when the cracks reached their current depth.

The current problem has three unknowns, namely the three principal stresses. It is therefore necessary to assume one of the stresses. It is selected here for the sake of illustration to set the vertical stress to 14 MPa, but any other option may be selected or a parametric analysis with respect to the vertical stress may be performed. If a bentonite pressure of 10 MPa is used and the depth of the cracks at the bottom of the borehole is 60 mm, the code yields a maximum horizontal stress of 27.3 MPa and a minimum one of 11.5 MPa.

8.5 Conclusions

The analysis performed in the chapter indicates that the fractures observed after dismantling in the frame of the BRIE project may well have been created by either disturbances in the stress field caused by the excavation of the tunnel and the drilling of the boreholes or by a combination of the above procedure with the swelling pressure of the bentonite parcels, as a result of the increase of their degree of saturation.

In addition, it is demonstrated how the approach can be used as an indication and guidance for increased understanding linking geological mapping, hydrogeological observations and possible (likely) rock stresses.

9. CONCLUSIONS AND FUTURE WORK

In this report a method for the evaluation of the borehole breakout shape was presented for the case when the properties of the intact rock and the *in situ* stress are known. An additional algorithm was described for the case when the breakout shape and the material properties are known and the *in situ* stress is sought.

The first algorithm was verified against analytical results and its applicability was validated against experimental results. The second algorithm was validated only against previous experimental results.

On the whole it can be concluded that both approaches provide good results for the respective application. The question of applicability for the evaluation of the *in situ* stress remains open, not due to the performance of the algorithm and the method developed for this project but due to evidence from experimental data. This evidence suggests that for certain types of materials and certain ranges of stresses at least, there may not exist a one to one relationship between breakout shape and stress state. Further research in this direction is required to provide a final answer to this question. This may require a suitable series of experimental results.

For the future it is planned to extend the capabilities of the code in three different directions: thermal effects, fluid flow and non-coaxial stress states. The first two extensions are straightforward, as they both correspond to classical fields of application for conformal mapping. The third requires some more effort, but the development is analogous to the one for the in-plane stress field discussed in the present report. The combined package could offer a simple and fast simulator for borehole stability.

A further step planned for the future is the repackaging of the algorithm on the basis of open source software. The code is currently implemented in Matlab. Implementing it in C with a Python frontend would significantly increase speed. In addition, in this manner it could be packaged and distributed as an executable with a user interface.

REFERENCES

Amitrano, D., & Helmstetter, A. (2006). Brittle creep, damage, and time to failure in rocks. *Journal of Geophysical Research: Solid Earth*, *111*(11). https://doi.org/10.1029/2005JB004252

Arzúa, J., & Alejano, L. R. (2013). Dilation in granite during servo-controlled triaxial strength tests. *International Journal of Rock Mechanics and Mining Sciences*, *61*, 43–56. https://doi.org/10.1016/j.ijrmms.2013.02.007

Cheatham, J. B. (1993). A new hypothesis to explain stability of borehole breakouts. *International Journal of Rock Mechanics, Mining Sciences & Geomechanical Abstracts*, *30*, 1095–1101.

Choens, R. C., Lee, M. Y., Ingraham, M. D., Dewers, T. A., & Herrick, C. G. (2019). Experimental Studies of Anisotropy on Borehole Breakouts in Mancos Shale. *Journal of Geophysical Research: Solid Earth*, *124*(4), 4119–4141. https://doi.org/10.1029/2018JB017090

Crook, T., Willson, S., Jian, G. Y., & Owen, R. (2003). Computational modelling of the localized deformation associated with borehole breakout in quasi-brittle materials. *Journal of Petroleum Science and Engineering*, *38*, 177–181.

Cuss, R. J., Rutter, E. H., & Holloway, R. F. (2003). Experimental observations of the mechanics of borehole failure in porous sandstone. *International Journal of Rock Mechanics and Mining Sciences*, *40*(5), 747–761. https://doi.org/10.1016/S1365-1609(03)00068-6

Exadaktylos, G. E., Liolios, P. A., & Stavropoulou, M. C. (2003). A semi-analytical elastic stress–displacement solution for notched circular openings in rocks. *International Journal of Solids and Structures*, *40*(5), 1165–1187.

Exadaktylos, G. E., & Stavropoulou, M. C. (2002). A closed-form elastic solution for stresses and displacements around tunnels. *International Journal of Rock Mechanics and Mining Sciences*, *39*, 905–916.

Fornberg, B. (1980). A numerical method for conformal mapping. *SIAM Journal on Scientific and Statistical Computing*, *1*, 386–400.

Fransson, Å., Åkesson, M., & Andersson, L. (2017). *Bentonite Rock Interaction Experiment*.

Fransson, Å., Lönnqvist, M., & Viola, G. (2019). Rock mechanical modelling of the Bentonite Rock Interaction Experiment, Äspö Hard Rock Laboratory, Sweden. *International Journal of Rock Mechanics and Mining Sciences*, *113*(April 2018), 255–267. https://doi.org/10.1016/j.ijrmms.2018.10.017

Gerolymatou, E. (2017). *Inherent and induced anisotropy in rock mass*. KIT, Karlsruhe.

Gough, D. I., & Bell, J. S. (1982). Stress orientations from borehole wall fractures with examples from Colorado, east Texas, and northern Canada. *Canadian Journal of*

Earth Sciences, *19*, 1358–1370.

Haimson, B. (2007). Micromechanisms of borehole instability leading to breakouts in rocks. *International Journal of Rock Mechanics and Mining Sciences*, *44*(2), 157–173. https://doi.org/10.1016/j.ijrmms.2006.06.002

Haimson, B., & Kovacich, J. (2003). Borehole instability in high-porosity Berea sandstone and factors affecting dimensions and shape of fracture-like breakouts. *Engineering Geology*, *69*(3–4), 219–231. https://doi.org/10.1016/S0013-7952(02)00283-1

Haimson, B., & Lee, H. (2004). Borehole breakouts and compaction bands in two high-porosity sandstones. *International Journal of Rock Mechanics and Mining Sciences*, *41*(2), 287–301. https://doi.org/10.1016/j.ijrmms.2003.09.001

Haimson, B., Lee, M., Chandler, N., & Martin, D. (1993). Estimating the state of stress from subhorizontal hydraulic fractures at the underground research laboratory, Manitoba. *International Journal of Rock Mechanics and Mining Sciences And*, *30*(7), 959–964. https://doi.org/10.1016/0148-9062(93)90052-F

Hakala, M., Siren, T., Kemppainen, K., Christiansson, R., & Martin, D. (2013). *In Situ Stress Measurement with the New LVDT-cell – Method Description and Verification*.

Herrick, C. G., & Haimson, B. C. (1994). Modeling of episodic failure leading to borehole breakouts in Alabama limestone. In *1st North American Rock Mechanics Symposium, NARMS 1994* (pp. 217–224). Austin, Texas: American Rock Mechanics Association.

Hoek, E., & Brown, E. T. (1980). *Underground excavations in rock*. London: The Institution of Mining and Metallurgy.

Janson, T., & Stigsson, M. (2002). *Test with different stress measurement methods in two orthogonal boreholes in Äspö HRL*.

Kachanov, M. (1994). Elastic solids with many cracks and related problems. *Advances in Applied Mechanics*, *30*, 259–445.

Kantorovich, L. V. (1933). On some methods of constructing a function effecting a conformal transformation. *Bulletin of the Academy of Sciences of the USSR*, *7*, 229–235.

Kargar, A. R., Rahmannejad, R., & Hajabasi, M. A. (2015). The stress state around lined non-circular hydraulic tunnels below the water table using complex variable method. *International Journal of Rock Mechanics and Mining Sciences*, *78*, 207–216.

Karnland, O., Olsson, S., & Nilsson, U. (2006). *TR-06-30 Mineralogy and sealing properties of various bentonites and smectite-rich clay materials*.

Lee, H., Moon, T., & Haimson, B. C. (2016). Borehole breakouts induced in Arkosic sandstones and a discrete element analysis. *Rock Mechanics and Rock*

Engineering, *49*, 1369–1388.

Lee, M. Y., & Haimson, B. . (1993). Laboratory study of borehole breakouts in Lac du Bonnet granite: a case of extensile failure mechanism. *International Journal of Rock Mechanics and Mining Sciences And*, *30*(7), 1039–1045. https://doi.org/10.1016/0148-9062(93)90069-P

Meier, T., Rybacki, E., Reinicke, A., & Dresen, G. (2013). Influence of borehole diameter on the formation of borehole breakouts in black shale. *International Journal of Rock Mechanics and Mining Sciences*, *62*, 74–85. https://doi.org/10.1016/j.ijrmms.2013.03.012

Michell, J. H. (1899). On the Direct Determination of Stress in an Elastic Solid, with application to the Theory of Plates. *Proceedings of the London Mathematical Society*, *s1-31*(1), 100–124.

Muskhelishvili, N. (2010). *Some basic problems of the mathematical theory of elasticity*. Springer.

Noll, W. (1972). A new mathematical theory of simple materials. *Archive for Rational Mechanics and Analysis*, *48*, 1–50. Retrieved from http://www.springerlink.com/index/M386414177201484.pdf

Papamichos, E. (2010). Borehole failure analysis in a sandstone under anisotropic stresses. *International Journal for Numerical and Analytical Methods in Geomechanics*, *34*, 581–603.

Savage, J. C., & Mohanty, B. B. (1969). Does Creep Cause Fracture in Brittle Rocks? *Journal of Geophysical Research*, *74*(17), 4329–4332. https://doi.org/10.1029/jb074i017p04329

Schinzinger, R., & Laura, A. A. (2003). *Conformal mapping: Methods and Applications*. Dover Publications.

Song, I. (1998). *Borehole breakouts and core disking in Westerly granite: Mechanisms of formation and relationship to in situ stress*. The University of Wisconsin - Madison.

Song, I., & Haimson, B. (1997). Polyaxial strength criteria and their use in estimating in situ stress magnitudes from borehole breakout dimensions. *International Journal of Rock Mechanics & Mining Sciences*, *34*(3–4), 116.

Stanchits, S., Surdi, A., & Gathogo, P. (2014). Onset of Hydraulic Fracture Initiation Monitored by Acoustic Emission and Volumetric Deformation Measurements. *Rock Mechanics and …*, *47*(5), 1521–1532. https://doi.org/10.1007/s00603-014-0584-y

Thörn, J. (2013). *Hydromechanical Behaviour of Fractures Close to Tunnels in Crystalline Rock*. Chalmers University of Technology.

van der Hoek, P. G., Smit, D.-J., & Khodaverdian, M. (1994). Material-dependent size effect of hollow cylinder stability: Theory and experiment. In *1st North American*

Rock Mechanics Symposium (p. ARMA–1994–0411). Austin, Texas: American Rock Mechanics Association.

Wawersik, W., & Brown, W. (1973). *Creep Fracture of Rock*. Retrieved from http://oai.dtic.mil/oai/oai?verb=getRecord&metadataPrefix=html&identifier=AD0775231

Zervos, A., Papanastasiou, P., & Vardoulakis, I. (2001). Modelling of localisation and scale effect in thick-walled cylinders with gradient elastoplasticity. *International Journal of Solids and Structures*, *38*, 5081–5095.

Zhang, H., Yin, S., & Aadnoy, B. S. (2018). Poroelastic modeling of borehole breakouts for in-situ stress determination by finite element method. *Journal of Petroleum Science and Engineering*, *162*, 674–684.

Zheng, Z., Kemeny, J., & Cook, N. G. W. (1989). Analysis of borehole breakouts. *Journal of Geophysical Research*, *94*, 7171–7182.

Zoback, M. D., Barton, C. A., Brudy, M., Castillo, D. A., Finkbeiner, T., Grollimund, B. R., … Wiprut, D. J. (2003). Determination of stress orientation and magnitude in deep wells. *International Journal of Rock Mechanics and Mining Sciences*, *40*(7–8), 1049–1076. https://doi.org/10.1016/j.ijrmms.2003.07.001

BeFo

Box 55545
SE-102 04 Stockholm

info@befoonline.org • www.befoonline.org
Visiting address: Sturegatan 11, Stockholm

ISSN 1104-1773